



HAL
open science

Archaeoseismological study of the Cherichira aqueduct bridge, Kairouan, Tunisia

Klaus-G. Hinzen, Mustapha Meghraoui, Nejib Bahrouni, Yassine Houla,
Sharon Reamer

► **To cite this version:**

Klaus-G. Hinzen, Mustapha Meghraoui, Nejib Bahrouni, Yassine Houla, Sharon Reamer. Archaeoseismological study of the Cherichira aqueduct bridge, Kairouan, Tunisia. *Mediterranean Geoscience Reviews*, 2021, 10.1007/s42990-021-00062-9 . hal-03483339

HAL Id: hal-03483339

<https://hal.science/hal-03483339>

Submitted on 17 Dec 2021

HAL is a multi-disciplinary open access archive for the deposit and dissemination of scientific research documents, whether they are published or not. The documents may come from teaching and research institutions in France or abroad, or from public or private research centers.

L'archive ouverte pluridisciplinaire **HAL**, est destinée au dépôt et à la diffusion de documents scientifiques de niveau recherche, publiés ou non, émanant des établissements d'enseignement et de recherche français ou étrangers, des laboratoires publics ou privés.



Distributed under a Creative Commons Attribution 4.0 International License



Archaeoseismological study of the Cherichira aqueduct bridge, Kairouan, Tunisia

Klaus-G. Hinzen¹ · Mustapha Meghraoui² · Nejib Bahrouni³ · Yassine Houla⁴ · Sharon K. Reamer¹

Received: 12 July 2021 / Revised: 11 September 2021 / Accepted: 11 September 2021
© The Author(s) 2021

Abstract

In the past, several destructive earthquakes have occurred in the North African Atlas Mountain ranges located along the Africa–Eurasia plate boundary. Although the region is rich with impressive archaeological sites, including those in modern Tunisia, few comprehensive archaeoseismological studies have been conducted. Historic sources account at least three damaging earthquakes in the Kairouan area in central Tunisia between AD 859 and 1041. Little is known about which faults triggered these earthquakes or the size of these events. The water supply of the city of Kairouan depended on a 32-km-long aqueduct with a large bridge (now partially collapsed) at the confluence of the de Mouta and Cherichira rivers. The original bridge of Roman construction was retrofitted twice during the Aghlabid period (AD 800–903) and probably in AD 995 during the Fatimid period. The ruined section of the bridge shows damage which might be related to the AD 859 earthquake shaking. Here, we present a detailed study of the history, the status and the damage of the Cherichira aqueduct bridge using previous historic accounts and written works, a 3D laser scan model, local geological and seismological characteristics, and include results of radiocarbon dating and a timeline of events. In addition to earthquake ground motions, we consider severe flash floods on the bridge as a potential cause of the damage. We estimate the severity of such flash floods and develop a model with 18 earthquake scenarios on local reverse and strike-slip faults with magnitudes between M_W 6.1 and 7.2. While a few damage patterns might be indicative of flooding, most damage can be attributed to earthquakes. It is highly probable that the earthquake in AD 859 caused enough damage to the Aghlabid bridge to render it dysfunctional; however, to resolve the question of whether another earthquake in AD 911 or 1041 caused the complete destruction of the previously retrofitted aqueduct by the Fatimids requires dating of additional sections of the bridge.

Keywords Archaeoseismology · Cherichira aqueduct · Kairouan · Historic earthquake · Flash flood · Laser scan · Dating · Synthetic seismogram

1 Introduction

Characterizing pre-instrumental earthquakes can be accomplished in part by the study of their effects on manmade structures from historical sources (e.g. Fréchet et al. 2008; Albini et al. 2013), archeological sites (Stiros 1988; Stiros

and Jones 1996; Hinzen et al. 2009) and earthquake surface breaks in the geologic record (e.g. McCalpin 2009). Utilizing field investigations, archaeoseismology, has been applied at numerous archaeological sites in the Mediterranean, particularly at the northern and the eastern parts (e.g. Stiros and Jones 1996; Stiros 2001, 2020; Psycharis et al. 2003; Meghraoui et al. 2003; Galadini et al. 2006; Marco 2008; Niemi 2017; Hinzen et al. 2018; Schweppe et al. 2021). Comprehensive archaeoseismological studies along the North African Mediterranean border are less frequent, despite numerous archaeological sites from the Strait of Gibraltar to the Nile delta. Tectonically, the region is characterized by the NNW–SSE trending convergence of the African and the Eurasian plate at 4–6 mm/year (Fig. 1; Bahrouni et al. 2020a).

✉ Klaus-G. Hinzen
hinzen@uni-koeln.de

¹ Department of Geosciences, University of Cologne, Cologne, Germany
² EOST-Institut Terre et Environnement de Strasbourg (UMR 7063), Strasbourg, France
³ National Office of Mines (Geological Survey), Tunis, Tunisia
⁴ National Institute of Meteorology of Tunisia, Tunis, Tunisia

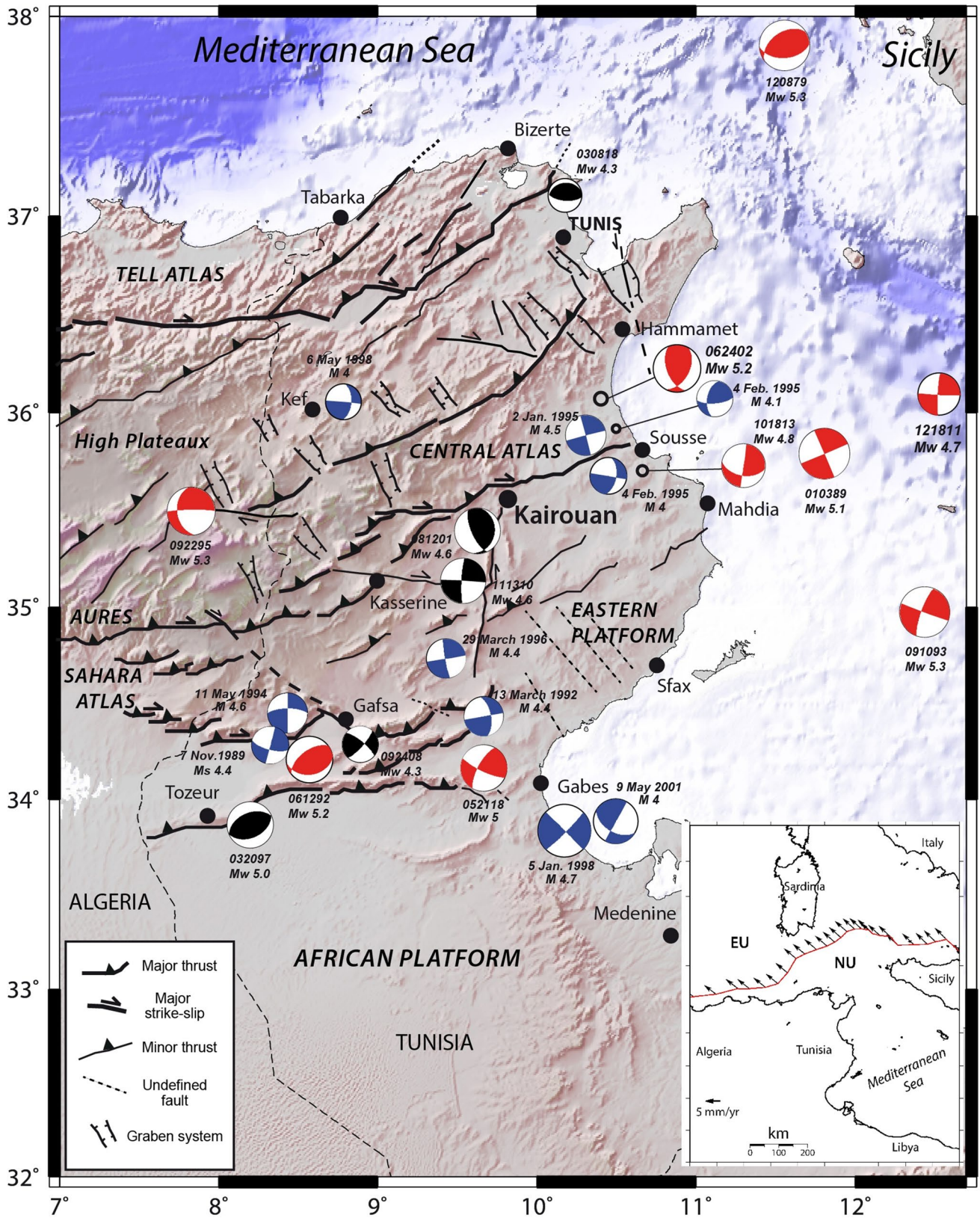


Fig. 1 Seismotectonic framework of Tunisia and surroundings (Bahrouni et al. 2020a, b). Focal mechanism solutions are from CMT-Harvard database (2019) (red), RCMT-INGV (n.d.) (black) and Institut

National Météorologie of Tunis (blue). The African–Eurasia plate boundary and convergence rate is in inset

Despite the relatively low convergence rate between the two plates in this western area of the Mediterranean, the region has been subjected to destructive earthquakes in the past (Mourabit et al. 2014). Kharrat et al. (2019) compiled a catalog of earthquakes in Tunisia, and Bahrouni et al. (2014) summarize the pre-instrumental earthquakes in Tunisia based on Roman and Arabic historic reports. In a recent paper, Bahrouni et al. (2020b) focus on an earthquake that occurred on October 9 in AD 859 which caused widespread damage in the city of Kairouan and surrounding environs (Fig. 1). At that time, the Kairouan City water supply depended in large parts on the discharge from the Cherichira aqueduct bringing in water from the 30 km NW distant Djebel Oueslet (Fig. 2). Aqueducts often extend tens or even hundreds of kilometers and thus are susceptible to earthquake ground motions that cross geologic environments and can even be caused by multiple active faults.

In their neo-tectonic and seismotectonic investigation of seismically active regions in Tunisia, Bahrouni et al. (2014) describe deformations of the Cherichira aqueduct bridge (CAB), a neuralgic spot of the aqueduct west of Kairouan (Fig. 2). They report that this aqueduct was built by the Romans and restored twice by Arabs, first during the Aghlabid period (AD 800–903) and second by the Fatimid (AD 909–969). Bahrouni et al. (2020b) further explore and date the effects of the AD 859 damaging earthquake in which among other locations affected the CAB and proposed that the earlier Bahrouni et al. (2014) interpretation of a direct faulting of the CAB does not appear to be valid and suggested further archaeoseismological investigations.

To further investigate potential causes of damage to the CAB, we carried out two field campaigns in 2019 in the Kairouan area. In this study, we will (1) document the current status of the CAB based on 3D terrestrial laser scans combined with digital photography and total station measurements; (2) describe damage patterns and repair phases; (3) discuss the amount of water in possible flash floods that could have affected the CAB; (4) show results of HVSR (Horizontal to Vertical Spectral Ratio) measurements at the CAB; (5) based on a new tectonic model of the Cherichira area, we use 18 earthquake scenarios to calculate synthetic seismograms for the site and intensity maps for a larger area including villages and the cities of Kairouan and Sousse affected by the AD 859 earthquake and possibly later historical earthquakes (Bahrouni et al. 2020b); and (6) use historic reports and additional physical C^{14} dating to establish a timeline of events from the middle of the 8th to the thirteenth century AD.

2 Aqueducts in archaeoseismology

Aqueducts are important infrastructures as they satisfy a basic but critical need for functioning of communities and cities. The very existence of an aqueduct or any other

artificial water system was a badge of city status. Without a reliable water supply, a town remained a mere rural hamlet (Brent 1984). A disruption to the delivery of water resulted in severe problems in daily life. Numerous examples from the present and past exist where earthquake ground motions have damaged lifelines. For example, two earthquakes in 2011 of magnitude M_W 6.2 and 6.0 heavily damaged the underground pipeline network of the city of Christchurch (New Zealand), disrupting water, wastewater, and gas distribution systems (O'Rourke et al. 2014). Another prominent example is the disruption of the water supply of San Francisco during the 1906 earthquake which partly increased the severity of fire damage due to a lack of firefighting water (Eidinger et al. 2006). Threats to long aqueducts during earthquakes include direct effects from fault movements and ground motions and secondary effects from liquefaction, differential settlement, lateral spreading, and slope deformation (Davis and O'Rourke 2011).

Several contemporary scholars have researched the hydrological achievements in Roman times (e.g. *Vitruvius* 1st cent. AD, *Lucretius* (97–55 BC), *Seneca* (4 BC–AD 65), and *Plinius Secundus* (AD 23–79). Within small settlements, water was supplied from cisterns and/or wells. When settlements grew to achieve city status, the demand for freshwater surpassed the capacity of local sources, not at least due to Roman bath culture. The problem was solved by the construction of aqueducts where possible. Often a military surveyor planned the route from a sufficiently productive well to the city limits. The canal was preferably constructed in a shallow trench; however, in certain situations, special works like tunnels, bridges, and siphons were added. None of these features were Roman inventions (Grewe 1986), and their uses have been well known since thousands of years; however, Roman engineers developed the technology to a standard never before reached. These include, in particular, aqueducts of more than 100 km length, cisterns with 20,000 m³ capacity, and aqueduct bridges of 50 m height. The dimensions of the water canal of aqueducts ranged between 0.4×0.35 m (e.g. Patara, Turkey) and 2.09×2.03 m (e.g. Manavgad, Sude, Turkey) (Grewe 1986). In later times, most of the Roman canals were large enough to be accessible for maintenance. The canals were constructed along the contours of the terrain; only if more economic, long diversions due to valleys were circumvented by building bridges (Garbrecht 1986). Aqueduct building material depended heavily on the availability of local materials and ranged from stone masonry and dressed stones to cast masonry and bricks.

Several archaeoseismological studies have shown that pre-instrumental earthquakes damaged aqueducts. Volant et al. (2009) examined the Nîmes Roman aqueduct in southeast France and found broken stalactites, arch warping, cracks and destruction of an aerial bridge, irregularity in the thickness of calcite deposits of the canal walls,

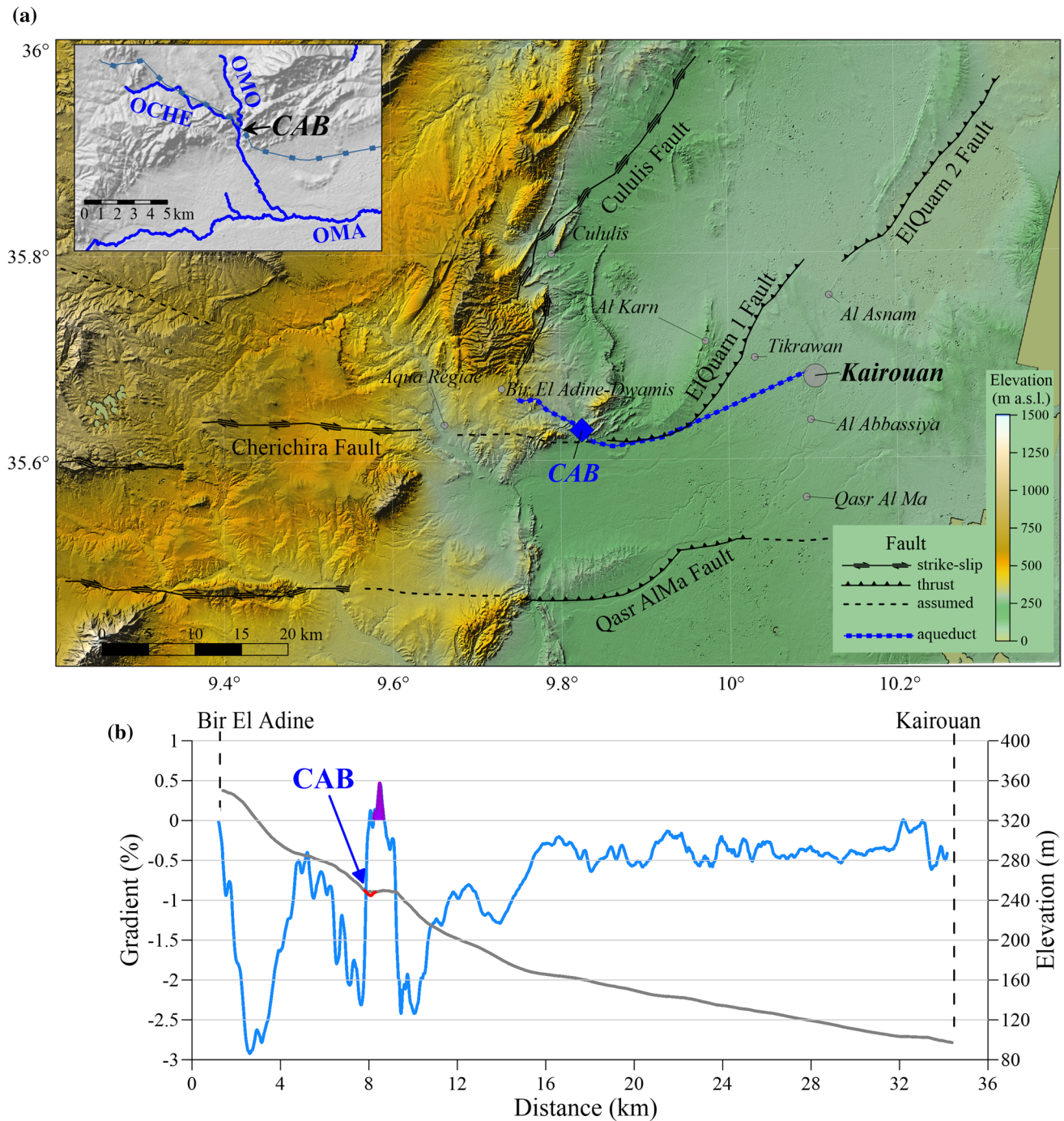


Fig. 2 **a** Morphotectonic of the study area based on ALOS World 3D–30 m Ellipsoidal (Takaku et al. 2014)). The blue line with squares shows the Cherichira aqueduct and the site of the bridge is indicated by a blue diamond labeled CAB. Tectonic faults and places affected by the AD 859 earthquake are indicated by black lines and gray dots, respectively. The insert on the lower right shows the color-

coded elevation levels. The small map in the upper left shows the surroundings of the CAB with the wadis *OCHE* Oued Cherichira, *OMO* Oued de Mouta, *OMA* Oued Marguelli. **b** The gray line gives the elevation along the aqueduct from the terrain model; the red section indicates the CAB. The blue line follows the gradient along the aqueduct. A short section with positive gradient is indicated in purple

the presence of numerous cracks, and a horizontal shift in the otherwise linear structure of the canal. The authors attributed all of this evidence of damage to earthquake ground motions. In contrast, they demonstrated that the

famous and still standing aerial bridge Pont du Gard was less vulnerable to the assumed local earthquake and thus survived without major damage.

DiVita (1996) showed that at Gortyn, capital of Roman an early Byzantine Crete, an earthquake had destroyed the pipeline network supplying the city with water, and the rich citizens constructed one or more branches of aqueducts to bring water back to the city.

The Al Harif Roman aqueduct, located on a segment of the Dead Sea fault in northern Syria, was subjected to successive left-lateral fault offsets with a total slip of 13.6 ± 0.2 m since the aqueduct construction (younger than 65 BC) documented by archeological excavations and paleoseismic trenches (Meghraoui et al. 2003). The combined analysis of trench results, tufa cores, and successive building and repair indicated four faulting events in the last 3500 years (Sbeinati et al. 2010).

Galadini et al. (2003) investigated a Roman tunnel in central Italy in the area that was struck by the 1997 Umbria-Marche seismic sequence. The 550-m-long and 2.5-m-high tunnel was constructed to drain a lake in the Colfiorito basin. To further answer the open question of the cause of the aqueduct collapse, some model calculations would be necessary.

The ~30-km-long Venafrum aqueduct in southern Italy retained a net vertical offset of almost 4 m at the intersection with a normal fault due to the occurrence of repeated large historical faulting that affected the Roman water supply (Galli et al. 2010).

Passchier et al. (2013) examined a 38-km-long Roman aqueduct at Ephesus in modern Turkey which was 3 m vertically offset and rendered unusable by a single normal faulting earthquake. A new canal was constructed as a partial repair on top of the damaged one. Dating of carbonate deposits places the event in the second century AD which occurred 35 years after operation. The authors mention that with more than 1400 ancient aqueducts in the Mediterranean (<https://www.romaq.org/>, last accessed March 2020), more archaeoseismological studies of these features should be performed.

A Roman aqueduct supplying the city of Antioch was studied by Benjelloun et al. (2015) who showed that earthquakes deformed the structure to such an extent, that water flow was reversed. Even though paleomagnetic and radiocarbon dating methods were applied, a conclusive identification of the damaging event(s) could not be resolved.

Hoffmann et al. (2019) examined vertical displacements of the 95-km-long Eifel aqueduct which supplied the Roman metropolis Colonia Claudia Ara Agrippinensium (CCAA, concurrent with modern Cologne) with water. At the so-called Holzheim Fault system, the authors found vertical offsets of the aqueduct of 15 and 35 cm, and signs of repair including a 4-km-long deviation from the original path to keep the aqueduct functional after the damage which probably was coseismic and occurred between 80 and 270 CE. An estimate of the earthquake size was not given by the authors; however, assuming 0.35 m as the maximum coseismic

displacement, the model by Wells and Coppersmith (1994) predicts a shallow earthquake of magnitude of M_w 6.3.

Sürmelihindi et al. (2021) did a detailed study of the carbonates from the 4th and 5th century AD aqueduct system of Constantinople which at a length of 426 km was the longest known water supply system of the ancient world. As the carbonate thickness covers less than 27 years of operation, they could deduce that the aqueduct was thoroughly maintained over the historically documented period of operation over at least 700 years. The final abandonment of the channel may have been due to an unrecorded earthquake, but a collapse of one of the major bridges at the end of the twelfth century due to lack of further maintenance is also possible.

While direct faulting of aqueducts due to earthquake permits unambiguous inference of seismic parameters, damage due to shaking cannot usually be directly interpreted and often requires detailed modeling of structures.

3 The Cherichira aqueduct bridge

3.1 Seismotectonic of the study area

Tunisia is tectonically divided into three regions from north to south. These include: (1) the NE–SW trending northern Tell Atlas with overthrusts and diapir structures, (2) the central and southern Atlas with E–W, N–S and NE–SW-striking thrust-related folds and NNW–SSE trending Neogene and Quaternary grabens, and (3) to the southeast the passive Sahel continental margin and eastern platform (Fig. 1). Deep-seated E–W trending right-lateral strike-slip faulting controls the NE–SW “en echelon” thrust-related folds across the Tell and Sahara Atlas (El Ghali et al. 2003). Although no coseismic surface faulting has been observed, and instrumental seismicity does not exceed M_w 5.4, the historical seismicity catalog lists earthquakes with VIII–X MKS intensity (Guidoboni et al. 1994; Ambraseys 2009; Kharrat et al. 2019). Focal mechanisms (Fig. 1) and neo-tectonic studies of the stress distribution show N–S to NNE–SSW shortening direction during the Plio-Quaternary across Tunisia Mountain belts and geological domains (Rebai et al. 1992; Bahrouni et al. 2014).

3.2 Historic earthquakes in the Kairouan area

Studies of historic earthquakes in Tunisia have been summarized and critically reviewed by Kharrat et al. (2019). They list two earthquakes in the Kairouan area, one in 854/55 (240 H) considered unlikely and another destructive seismic event in AD 912. Table S1 in the electronic supplements lists important earthquakes in Tunisia. Based on historic documents, Bahrouni et al. (2020b) showed that the former earthquake actually occurred on 8 Rajab 245 in the Hijri

lunar calendar which corresponds to the 9 October AD 859 in the Gregorian calendar. An additional earthquake in 432 H (Sep. AD 1040–Aug. AD 1041) affecting the Kairouan area listed by Ambraseys (2009) is potentially also relevant for the fate of the CAB. Ambraseys (2009) quotes al-Umari f.53v. “In the year a.H. 432 a great earthquake occurred at Kairouan and in North Africa. Part of the town of Kairouan was swallowed up, smoke rising up from the cavity”. Considering the severe earthquake damage and related intensity distribution, the seismic hazard study of Tunisia made by Ksentini and Bouden-Romdhane (2013) estimates a 3 m/s^2 PGA for the Kairouan area at an exceedance probability of 10% in 475 years.

3.3 The Cherichira aqueduct

The Cherichira aqueduct was built to transport water from the Djebel Oueslet, a segment of the Tunisian Atlas thrust front, to the city of Kairouan and later further to Sabra al-Mansurya (Mahfoudh et al. 2004) comprising a total length of ~32 km (Fig. 2). It was originally constructed during Roman times (Mahfoudh et al. 2004), but was often damaged and repeatedly retrofitted, in particular between the eighth and tenth century AD. The aqueduct starts at Bir el Adine at an elevation of 356 m (Fig. 2b). Several smaller canals collect water from diverse springs along the first 5 km of the aqueduct. The hydraulic features in the region were extensively explored by Gauckler (1900). In a sketch in his report, he shows four main contributing canals. However, the canals meet in the ~5.5-km-long section upstream of the CAB which was necessary to span the valley of the Oued (river) el Mouta, a tributary from the left bank of the Oued Cherichira, a tributary to the Oued Marguellil (Fig. 2). Depending on the terrain, the canal was buried in some parts and open in others. At several places, remains of two parallel canals, potentially Roman and Aghlabid, exist (Bahrouni et al. 2020a, b); its size in general is about 0.8 m wide and 1.2 m high. Downstream from the bridge, the aqueduct leaves the mountain range. After another kilometer, the trend of the flow direction changes from SE to E and then to ENE and reaches the city limits of Kairouan in five straight sections in the form of an underground canal after 25 km.

The local gradient shown in Fig. 2b was calculated by the differentiation of the elevation from a digital terrain model (ALOS World 3D–30 m Ellipsoidal, Takaku et al. 2014; Tadono et al. 2014) along the canal which itself was digitized from the Tunisia topographic map (1:50,000, sheet 63, Kairouan). As the canal is in large parts buried, the gradient of the canal itself does not necessarily fully agree with the gradient of the terrain. However, at the CAB and the next kilometer immediately downstream from it, the gradient significantly lessens (a short section even indicates a positive terrain gradient, Fig. 2b). Any elevation change due to

tectonic movements along this section of the aqueduct would have been critical for its functioning.

The terrestrial laser scan described in detail in the following section was primarily made to capture the current status of the CAB; however, as all scans were made with a horizontal cover of 360° , the surrounding terrain was also captured. The raw scan, which consists of 150 Mio. points covering an area of $250 \times 70 \text{ m}^2$ along the bridge, was used to extract a digital terrain model (Fig. 3a). The point cloud was sliced in 1-m-wide stripes and vegetation and artifacts were deleted manually from the profiles of each of these stripes. Subsequently, the cleaned elevation data were recombined and a model created with a Kriging algorithm. Two profiles parallel to the bridge show the 12.6 m incision by the Oued el Mouta which had to be bridged for the water canal (Fig. 3b).

3.4 Current status of the aqueduct bridge

The current status of the Cherichira aqueduct bridge (CAB) was documented with the 3D terrestrial laser scan. Figure 4a shows an orthographic view from SW towards the 180-m-long section of the CAB together with a plan view in Fig. 4b. The bridge is located at 35.6307°N and 9.8260°E (northern end); the section shown in Fig. 4a contains 37.5 Mio. points. A total of 29 scanner positions along the western and eastern side of the aqueduct were combined to construct the full model. The trend of the modeled section is $\text{N}131^\circ\text{E}$. The biggest challenge for the scanning procedure was the over-abundant vegetation of high grass, bushes and small trees, only some of which were removed during the two field campaigns.

In the following, the explored part of the CAB is divided into nine sections labeled A to I from NW to SE, where B, D, and F are gaps without major visible remains of the original construction (Figs. 4 and 5). The height of the ruins aboveground in section A increases from NW to SE from 1.5 m to 4.3 m due to sloping terrain. Section C shows severe damage, and the remaining height aboveground is about 2 m. Some 5 m south of section C, a small fraction (C1) extrudes from the slope within the gap labeled D; however, the elevation of C and C1 differs by at least 4 m from rest of the bridge. In the neighborhood of C and C1, several large debris piles are visible within the bushes, including remains of a water channel. The best-preserved part of the bridge in section E has a maximum remaining height above the (current) ground of 11.1 m. Towards the SE, the height decreases as dictated by the natural slope to about 2.7 m. Section G rises to 2.2 m aboveground and then descends in section I to about 1.1 m. Section H was heavily overgrown by shrubs, and the estimated existing height is 1.4 m. Table 1 summarizes the dimensions of the sections.

Section A (Figs. 4b and 5a) is the most northern of the examined area of the CAB. It is roughly 30 m long, the

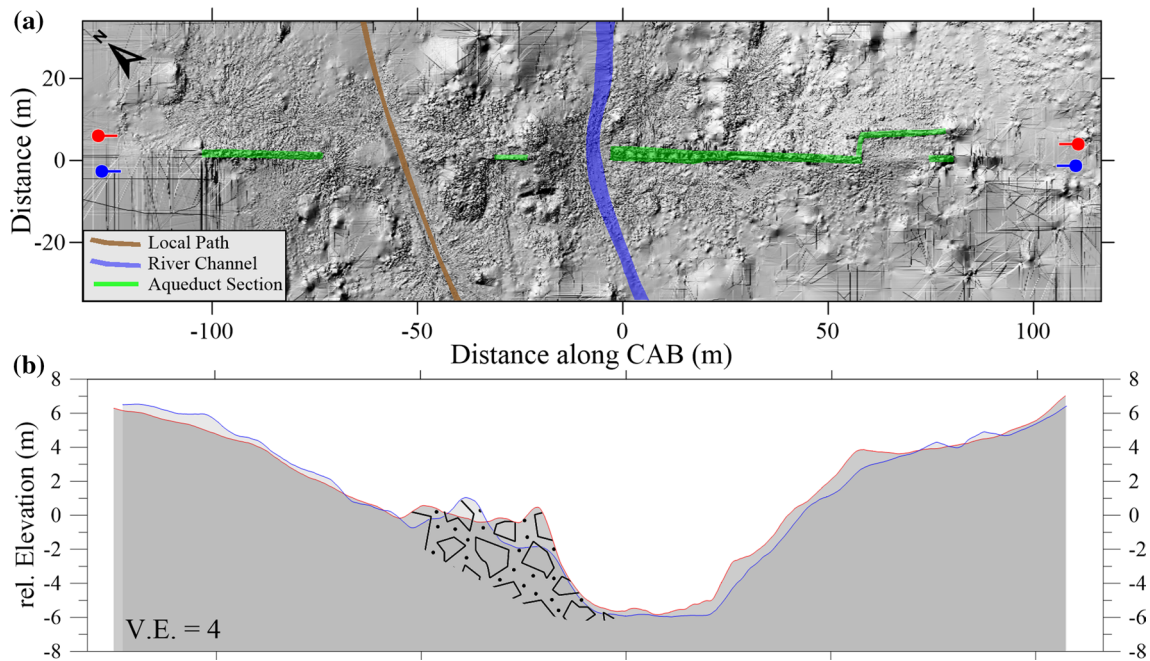


Fig. 3 Topographic situation at the CAB. **a** The digital elevation model was produced from the terrestrial laser scan of the bridge; the remains of the CAB are highlighted in green, the base of the river channel in blue, and a path in brown; the red and blue markers give

the trend of two profiles north and south of the CAB which are shown in **(b)**. The hatched part indicates a pile in section C containing a lot of debris from the bridge

height of the remains aboveground is ~ 1.5 m and 4.3 m at the northern and southern end of the section, respectively, and the width at its top is 1.49 m. On both sides of the wall, about a dozen niches exist. These are 1.0-m wide, 0.75-m high and 0.3–0.5-m deep. The average distance between niches in section A is 2.17 ± 0.15 m. At the southern end of section A, massive fractures cut almost vertically throughout the structure, accompanied by several centimeter-thick tufa deposits.

Section B is the more than 40-m-long gap between sections A and C (Figs. 4b and 5b). While it contains some rubble and heavily degraded parts of the aqueduct, the vegetation prevented a more thorough study of this section.

In section C, the canal of the aqueduct is at a much lower level (~ 4.8 m) than along the rest of the bridge and at its top it has only a width of 1.0 m (Figs. 4b and 5c), less than in all other sections. The visible water channel is 0.47 m wide. Most parts of the channel in section C are filled with mortar and stones which pack the channel without any gaps. Thin tufa layers at the channel walls show that it was in use for only a limited period of time. The fill must be younger than the active period of this section of the canal, and was probably part of some constructions on top of the filled canal. There are several features which indicate that damage in section C was repaired at one point in the history of the bridge. One of these features is the ruins of (at least) two 1.0-m-wide buttresses on the western side of the section

with a 6.15-m-wide gap in between; no evidence exists for a masonry bond to the wall they support, a sign which could indicate a later addition to give the canal support. Later, the buttresses collapsed together with the canal. In Fig. 6a and b, one of the buttresses is indicated by the red shading. Another sign of repair is a part of section C which shows clear trowel lines on both sides of the wall, filling a stretch of at least 3 m length and minimum 1 m height. This type of construction has not been found anywhere else along the scanned section of the CAB and could be attributed to a repair, possibly together with the buttress construction. Further indicated in Fig. 6b are major cracks, some of which trend along the edge of the inserted part with the trowel lines and one with tufa deposits on the outside of the wall.

At the base of section C, blocks are visible which indicate the top of an arch so that the original construction would have had more than the remaining four arches. However, further excavation is needed to clearly deduce the nature of this structural element.

The distances between three niches on the western side of section C are 2.97 m and 3.12 m, corresponding well with the gaps between the niches in section E, evidence that both might be from the same construction period.

The small mound which holds the remains in section C and the large chunk of the wall C1 contains a lot of debris of the bridge, indicated in the profiles in Fig. 3b. Large broken parts of the wall and canal fragments are scattered at

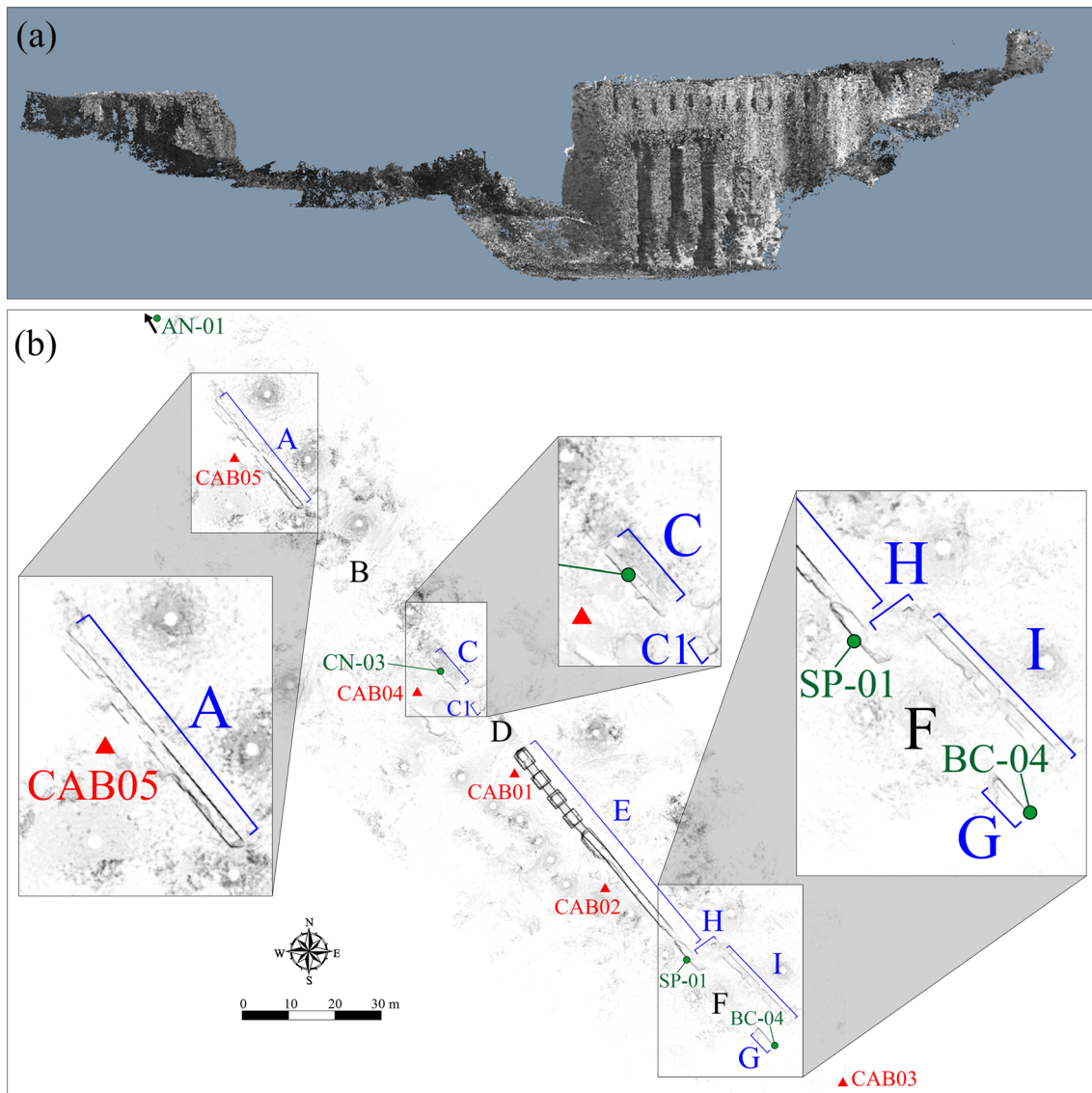


Fig. 4 **a** Perspective view from NW to the CAB 3D scan model. Total length of the model is 180 m. **b** Overview map of the scanned Cherichira aqueduct. Individual sections are marked with blue capital letters starting from NW; black letters indicate the gaps between sections. An arrow on the top left points towards a small pool about

100 m outside the map area. Three zoom-windows show more details; the scale bar applies to the main map; the labeled red triangles mark positions of HVSR measurements and the labeled green dots give locations of C14-dating samples

the surface east of the bridge, and a broken-off section of the canal is visible in a small trench which had before been excavated west of section C.

Section D is the gap between sections C (C1) and E including the lowest part of the Oued el Mouta valley which the CAB crosses. The distance between the southern end of C1 and pillar 1 in section E is about 11.5 m (Figs. 4b and 5d). This gap includes a path at the bottom of the valley; however, no traces of pillars north of pillar 1 in section E are currently visible.

The most spectacular part of the CAB is section E with the remains of four arches and the corresponding pillars

(Fig. 4). The pillars are denoted 1–4 (Table 2) starting with the most northern one. The average dimensions of the pillars were (due to irregular edges, especially the more damaged areas) measured from a top orthographic view to the scan of the bridge (Fig. 7). Table 2 gives the size and an estimate of the height up to which the edges are damaged and the width additionally in units of Roman *passus* (metric equivalent to 1.48 m).

Figure 7a shows a photo of the bridge seen from the west (building dimensions reported in Table 2). Pillars 2, 3, and 4 show similar dimensions (as also with the four gaps between pillars); however, the first pillar (from the left) is of different



Fig. 5 View from west to sections A (a), B (b), C (c), and D (d) of the CAB 3D scan model

size. While the width in EW direction of 2.90 m (~ 2 *passus*) agrees with the other three pillars, the extension in NS direction (parallel to the trend of the bridge) is at least 3.98 m, and thus diverting significantly from the almost square cross section of the other pillars. As seen in Fig. 7b and c, the northern face of pillar 1 is a breaking edge supporting the reconstruction suggested by Gauckler (1900) which infers that pillar 1 extended all the way to the northern riverbank, similar to the substructure at the southern side. A supporting argument for this assumption comes from the construction of the edges of all pillars (including the southern face of

pillar 1). While large areas of the faces of the bridge are made from crude field stones, the edges are built from somewhat larger typical Roman-worked rectangular ashlar, often placed alternately in a horizontal and vertical direction. No traces of such ashlar remained at the northern face of pillar 1.

As viewed from the ground, the top part of section E gives the impression of waviness with a large wavelength almost as long as the section itself. Such waviness could be interpreted as a sign of seismic loading. A map view of the scan model of this section (Fig. 7b) shows that the

Table 1 Size of the individual section of the scan model of the Cherichira aqueduct bridge

Section	Length (m)	Width (m)	Height (m)	Canal width (m)
A	29.71	1.49	1.50–4.30	0.67
B	40.30	N/A	N/A	N/A
C	11.92	0.995	~2.0	0.47
C1	2.40	1.20	~1.4	N/A
D	18.20	N/A	N/A	N/A
E	60.68	1.49	11.10–2.70	0.57
F	15.18	N/A	N/A	N/A
G	4.14	2.0	2.20	0.8
H	7.32	N/A	1.40	N/A
I	23.0	1.44	1.10	0.38

“waviness” is only in the top part containing the water channel, with a total height of ~2.5 m (superstructure). The pillars are in the trend of the substructure which is built against the southern slope of the hill. While the substructure and the pillars are about 2.90 m wide, the superstructure with the water channel is only 1.5-m wide. At the southern end, the eastern side of the substructure and the superstructure are

aligned. But towards pillar 4, the superstructure is curved and meets pillar 4 as well as the following three pillars in their middle. This indicates that the superstructure was adjusted in its trend during the construction on top of the existing substructure and pillars, so the channel would be centered on the pillars; a post-construction deformation of the superstructure is unlikely, thus negating a seismogenic cause for this bending of the channel.

A regular pattern of niches exists on both sides of the bridge (Fig. 7). The top of the niches is about 1.0 m below the upper rim of the remaining bridge and the average distance between the niches above the arches is 3.10 ± 0.16 m and with width and height of 1.0×0.70 m.

South of the fourth arch in section E, the bridge meets the natural slope of the left bank of the Oued el Mouta (Fig. 2). The 2.9-m-wide substructure extends for ~6.5 m south of the fourth arch, and it functions as the base for the 1.5-m-wide upgoing wall with a water canal on top. As shown in Fig. 8a, the border between the two units is irregular. Where the western shell of the construction crumbled, some spolia of fragments of an old water canal with a layer of *opus signinum* (watertight Roman building material) and some attached tufa is visible (Fig. 8b

Fig. 6 View from west to section C. **a** Colored 3D scan, **b** same view as in (a) with a buttress shaded red, tufa deposits in yellow and a segment of the wall with trowel lines in blue. Red lines mark major cracks in the wall



Table 2 Dimensions of the remains of the bridge of the Cherichira aqueduct

Pillar	Width NS (m)	Width NS (passus)	Width EW (m)	Width EW (passus)	Gap (m)	Height Arch (m)	Damage h (m)
1	> 3.98	> 3.09	2.90	1.96	2.40	7.86	2.55
2	2.97	2.01	2.87	1.94	2.46	7.81	3.58
3	2.90	1.96	2.88	1.95	2.44	7.78	2.85
4	2.93	1.96	2.88	1.95	2.42	7.84	4.60

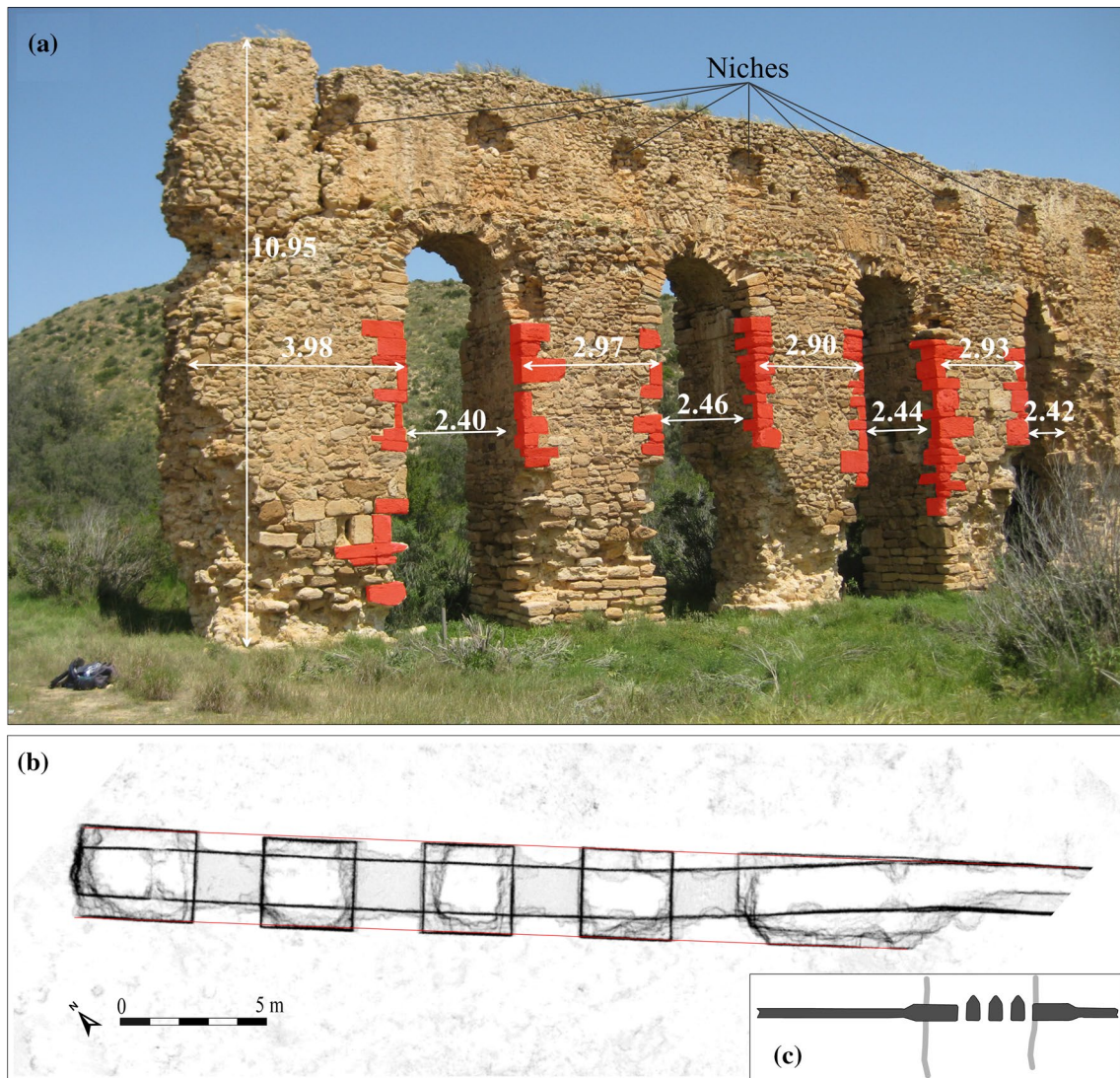


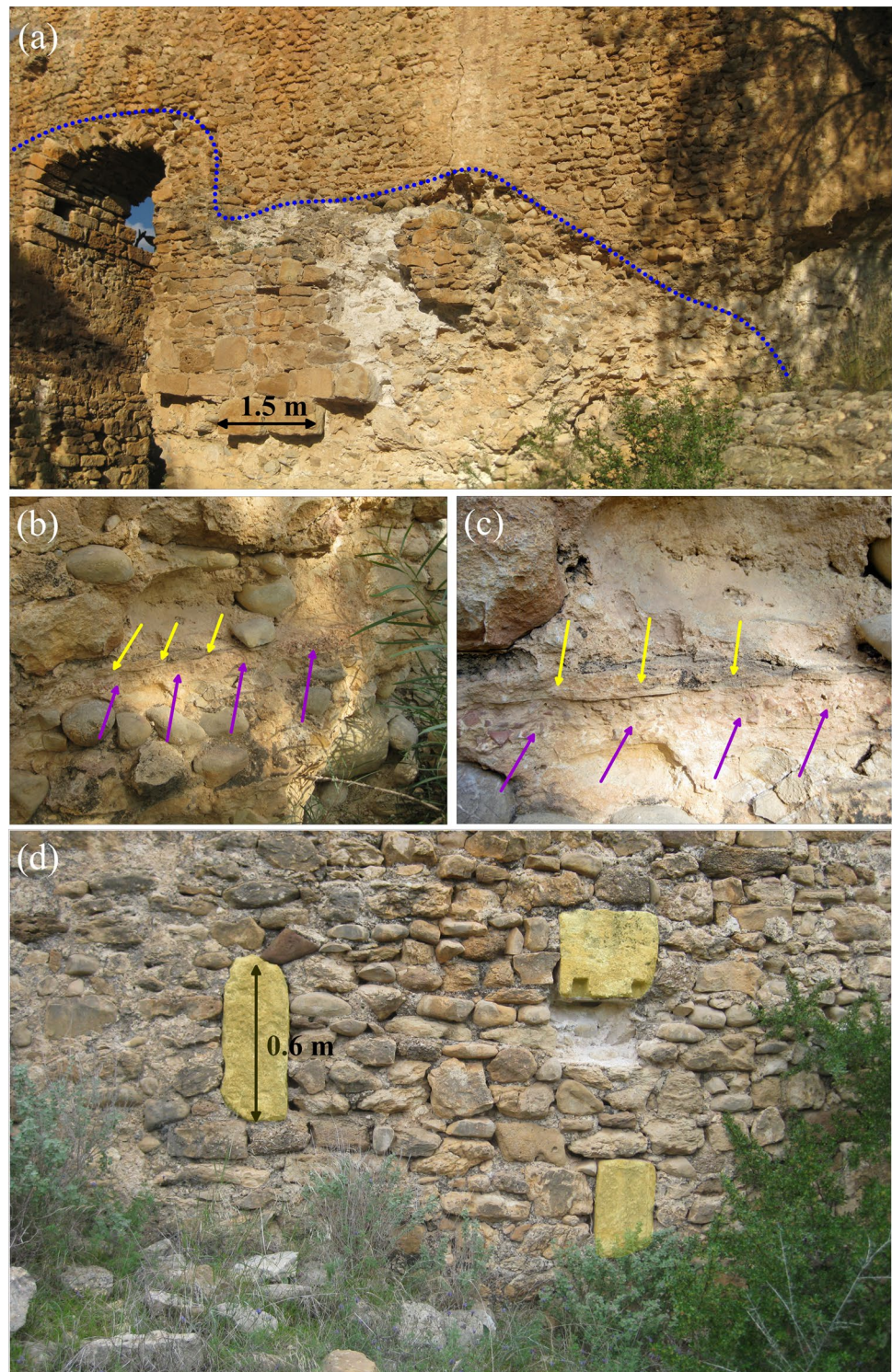
Fig. 7 **a** Photo of the western side of section E of the CAB; all measures given in meters were taken from the laser scan model. Larger worked ashlars at the pillar-edges are indicated in red. **b** Orthographic top view of the scan of the pillars in section E which appear as black rectangles. The two parallel red hairlines are straight and fitted to the

southern part of the base, black lines indicate the trend of the curved top part of the bridge with the water channel. The insert **c** shows the ground plot following the reconstruction of Gauckler (1900) (photo K.-G. Hinzen)

and **c**). On the eastern side of the bridge, some large worked ashlars, probably of Roman origin, are found within the outer shell of the wall which is otherwise

made from crude stones (Fig. 8d). In the river bed, south of the bridge, we also found a large fragment of a Roman column.

Fig. 8 **a** Photo of the western side of section E of the CAB with the most southern arch at the left side. The dotted blue line shows the border between the 3.0-m wide substructure and the narrower 1.5-m wide wall on top. The photos in **(b)** and **(c)** show some spolia visible in the parts, where the outer shell of the wall broke off. Pink and yellow arrows point to remain of water tight canal lining (*opus signinum*) and attached tufa deposits, respectively. The photo in **(d)** was taken on the opposite (eastern) site of the bridge; the yellow shade indicates three large blocks used as spolia (photo K.-G. Hinzen)



Section F is the gap between the southern end of the bridge, section E and section G (Fig. 4b). Here, the trend of the aqueduct structure is well visible on the ground surface; however, the structure is leveled to the ground with no rising wall remains.

Section G (Fig. 4b) shows two distinct differences to the rest of the ruins of the CAB: (1) the wall is wider (~2.0 m) compared to the other sections, and the canal with ~0.8 m width is larger. The elevation of the canal does not fit the elevation of all other sections, e.g. the water channel in section

G is ~1.0 m higher than the one in neighboring section I. Gauckler (1900) interpreted section G as a remain of a later (Fatimid) bridge canal compared to the narrower (~0.38-m wide and ~1-m lower) Aghlabid bridge canal in section I. But except for section G, no remains of a 1-m higher canal exist.

Section H constitutes a short deviation and connection between section E and I with a trend nearly perpendicular to the other two sections (Fig. 4b). Section I then continues with a common trend (N131°E), but about 5.5 m further east along a line connecting the bridge (section E) and section G (Fig. 9a–d). Section I shows heavy damage; in particular, segments of the western side of the water canal broke away and were shifted westward by ~0.22 m, but are still in place (Fig. 9c and d). Three cracks cut through the whole canal causing warping, a damage pattern that could well be of seismogenic origin.

3.5 Tufa deposits and spilling

Previous studies (e.g. Meghraoui et al. 2003; Passchier et al. 2013; Sürmelihindi et al. 2021) have shown that tufa deposits can be helpful to uncover the history of aqueducts as they record the periods of active operation and can be physically dated. Sections A, C, and E show calcite (tufa) accumulation in several places where water spilled down the sides of the aqueduct (Fig. 10) and the thickness and extent of the tufa deposits on the walls indicate that this spilling probably lasted decades. This observation is supported by the local name “Cherichira” given to the site which translates to “water cascade”.

Most of the major spills are bound to major cracks, some of which cut through the complete aqueduct wall, but overflow also occurred at locations without major cracks where

thick (several decimeters) mixed tufa, organic and silt deposits exist in the water channel. These deposits, indicating a lack of maintenance, might have been the cause for some spills, but this interpretation would have to be verified with a thorough cleaning of the water channel and mapping and dating of the tufa deposits. To reveal the formation process of the cracks is a major goal of future dynamic models of the CAB.

3.6 Gradient measurements

To function efficiently, a minimum gradient has to be present along the whole length of an aqueduct to secure water flow without overflow; too large of a gradient will increase wear and tear of the construction. As it is not clear at this point how sections E and G were connected to the upstream section A, we deduced the gradients of the CAB from the scan data. *Vitruvius* recommended a gradient of 0.5% and *Plinius Secundus* one as low as 0.02%. Actual Roman aqueducts have values between 0.3% and 0.15% with extremes of 0.07–3% at Nimes and Roma, respectively (Matthews 1970). With the presence of sufficient head of water between a source spring and a city, aqueducts followed the terrain (even with changing gradients) for economic reasons. However, in case of small height differences, canals often contained constant, small gradients over long stretches. The Kaikos aqueduct supplying Pergamon, for example, had a gradient of 0.3‰ (0.3 m height difference over 1 km) over a stretch of 50 km (Garbrecht 1986). The well-studied 94-km-long Eifel aqueduct, which supplied Cologne with fresh water, had extreme gradient values ranging from 0.10% to 9–10% (Grewe 1986).

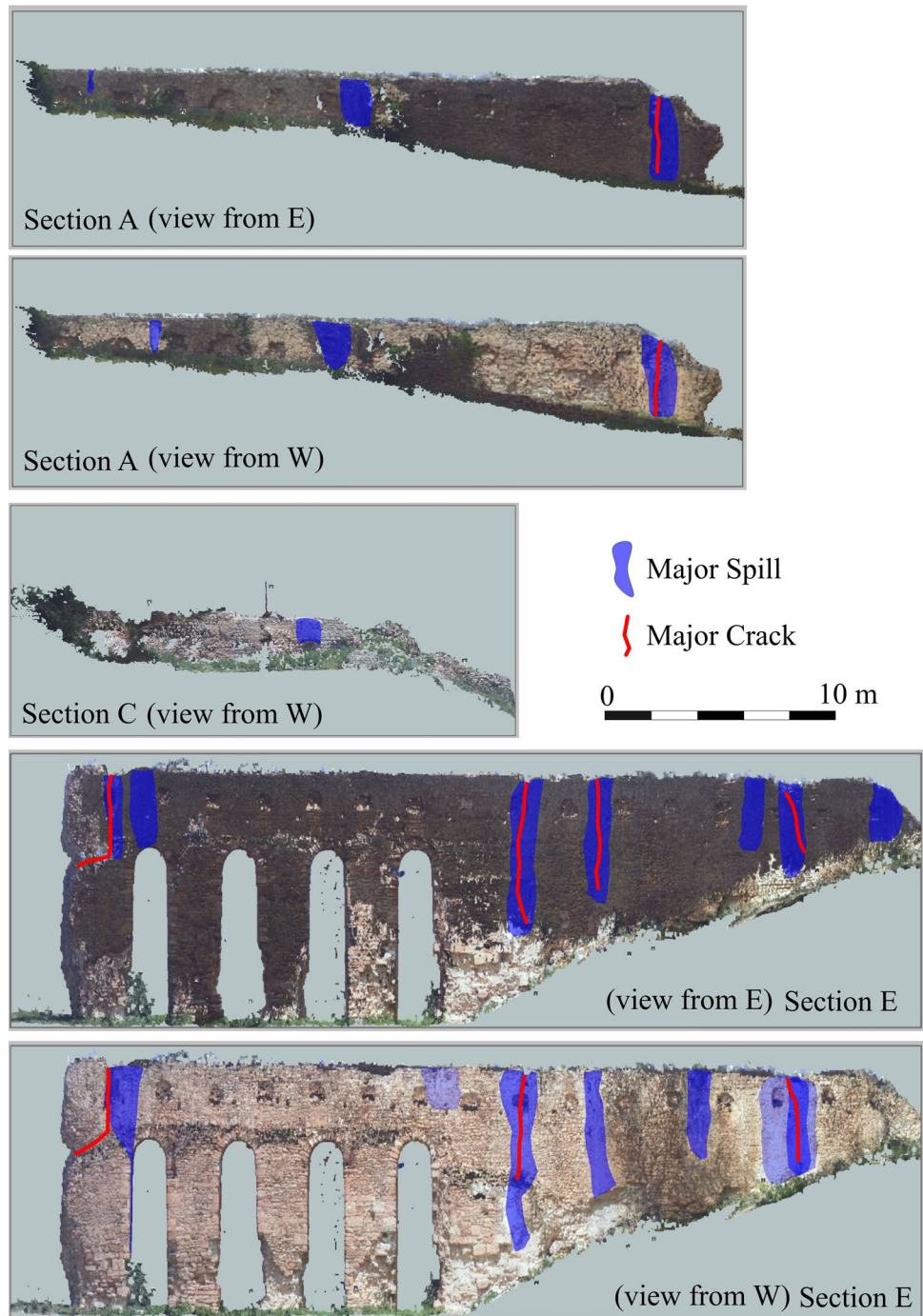
Gradients along the CAB were measured from orthographic crosscuts of the scan model (Fig. 11a and b). In



Fig. 9 Planar views to the laser scan of sections F–I at the southern end of the CAB. **a** View towards south along section F to section G; **(b)** oblique view to sections F and G; **(c)** eastward view to section I,

section H is hidden under the shrubs on the left side; **d** view in flow direction towards south along section I, the red arrows indicate a 0.22 m shift of the broken western wall of the canal

Fig. 10 Orthographic view to sections A, C, and E of the CAB; view direction is indicated on the bottom of each graph. The views from E have been flipped horizontally to match the positions of the views from W. Major spills with tufa deposits on the walls and major cracks are indicated



general, the top parts were selected for the measurements since a clear view to the canal base did not exist in all sections (i.e., for security reasons we did not scan the top of section E). However, the 1.0-m-height difference between sections G and I could be inferred from a cross-cut perpendicular to the trend of the aqueduct directly from the base of the canals. Table 3 gives the height and lateral distances of the measured endpoints of the sections. Connecting the

northern end of section A and the southern end of section E with a straight line shows a good fit to most remains of the aqueduct. The overall gradient of this section is 1.40%. However, as shown in Fig. 11a, the top level of section C is ~5.0 m below the connection line of A and C, and the top of G is 1.0 m above it. If A and G are connected directly, the gradient is reduced to 0.35% a value that better fits the Roman design rules than the A–E gradient.

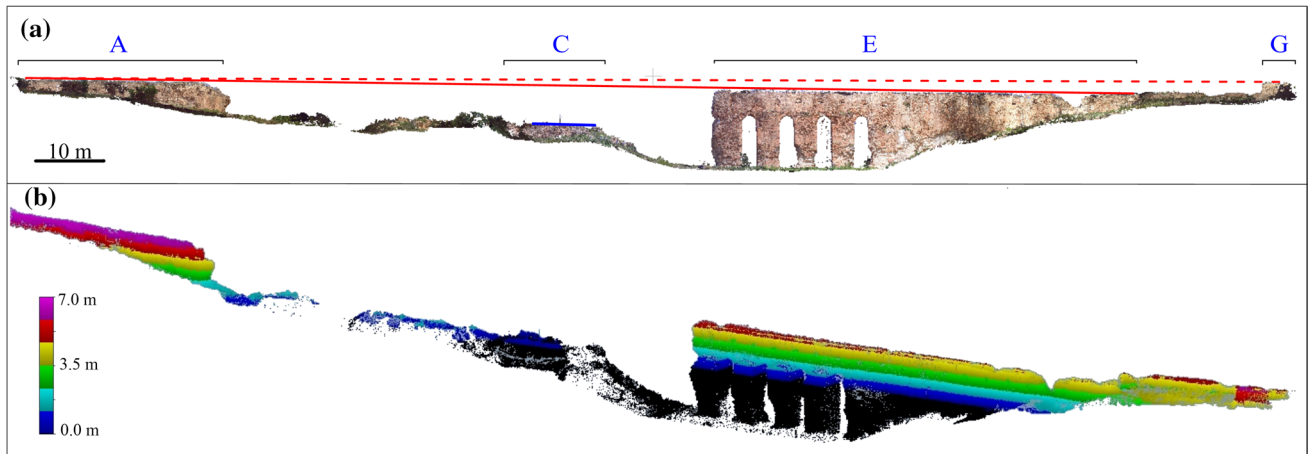


Fig. 11 **a** Orthographic view of the scan model of the CAB from west. Blue labels indicate the sections of the bridge. The continuous and dotted red lines connect the northern end of section A the southern ends of sections E and G, respectively, with a gradient of 1.4%

and 0.35%, respectively. The blue line marks the current top of section C. **b** Perspective view to the point cloud of the scan of the CAB from west with color coding of the relative elevation of the top part of the structure; elevation scale is given in the lower left corner

Table 3 Evaluation of the gradient of sections and average intersection sloping

Section	dz (m)	dx (m)	Slope (deg)	Gradient
A-E	2.16	154.01	0.80	1.40%
A-I	1.94	166.72	0.67	1.16%
A-G	0.625	176.38	0.20	0.35%

dz elevation difference, dx distance along bridge

3.7 Estimate of flowrate at the CAB

Gauckler (1900) assumed, that the Fatimid retrofitted the Aghlabid aqueduct to meet an increased water demand in Kairouan. The capacity of the two canals can be estimated with the so-called Gauckler–Manning–Strickler formula (e.g. Chow 1959); the flow velocity v_m is:

$$v_m = k_{st} \cdot \sqrt[3]{R^2} \cdot \sqrt{I} \tag{1}$$

with $R = A/U$

Input parameters are the cross section of the here rectangular shaped canal A , the wetted extend U , the slope I , and the Strickler-coefficient k_{st} . The latter is determined by the roughness of the canal walls. For a canal with an old

concrete lining, a k_{st} of $60 \text{ m}^{1/3}/\text{s}$ can be assumed (<https://www.gabriel-strommer.at/en/calculators/flow-velocity-flow-rate/>, last accessed March 2021). Table 4 lists the estimated values of a capacity, assuming the canals in sections I and G, respectively, are filled to half their height and shows a threefold capacity of the Fatimid CAB canal compared to the Aghlabid CAB canal.

3.8 HVSR measurements

Measurements of ambient noise at five locations (CAB01–CAB05, Fig. 4b) were made to determine horizontal to vertical component spectral ratios (HVSR); these can give some basic ideas of the frequency of ground amplifications due to soft surface layers (e.g. Mucciarelli and Gallipoli 2001; Lunedei and Malischewsky 2015). Measuring procedure and results are given in the electronic supplements (Fig. S1). Except for an impedance contrast correlated to the base of the sediment fill in the wadi center, no indications for major site effects were found.

As shown in the inset of Fig. 7c, following the reconstruction inferred by Gauckler (1900), there is good reason to assume that the pillars are of Roman origin with a protecting triangular shaped abutment pointing upstream, typical for a Roman construction (e.g. Alcantara Bridge, Spain; Pons

Table 4 Estimate of the water flow rates for a half-filled Aghlabid and Fatimid canal at the CAB

Canal	Cross Section A (m ²)	Wetted extend U (m)	Gradient (%)	Flow velocity (m/s)	Flow rate (m ³ /s)	Capacity (m ³ /day)
Aghlabid	0.08	0.8	1.40	1.5	0.12	10,540
Fatimid	0.28	1.5	0.35	1.2	0.33	28,080

Aemilius, Italy; Trajan's Bridge, Rumania; Pont di Gard, France). Mahfoudh et al. (2004) also describe the existence of the abutments being in the *Vitruvian* tradition. If such abutments exist under the current sediment cover, it is logical that they were found on solid ground and that the 2–3 m soft layer indicated by the HVSR measurements is the fill of the wadi (to be confirmed by excavations) and does not contribute to earthquake site effects to the bridge.

3.9 Physical dating

Bahrouni et al. (2020b) published the results of two radiocarbon (C^{14}) dating samples which were taken from an exposed cross section of the buried water canal ~ 800 m south of the CAB. One sample (KAI AQ N3) was taken from the *opus signinum* lining of the canal, the other (CHER3) from the bottom part of silt and sandy sediments that began to fill the canal after its abandonment and thus bracketing the time of its dysfunction. In the second field campaign in 2019, we collected more samples of charcoal imbedded in the mortar of several parts of the CAB (Fig. 4b). Sample BC-04 was taken from mortar of the wall immediately below the canal in section G; SP-01 was taken from the wall at the southern end of section E; and CN-03 from the cement lining in section C. A further sample (AN-01) was taken from cement of a small round pool about 100 m north of section A. Figure 12 shows the results from all samples currently available and Table S2 in the electronic supplements summarizes the results. A sample taken from the base of one of the pillars turned out not to be dateable; however, the available dates confirm significant interventions at the CAB since the ninth century AD.

3.10 Summary of main CAB features

The main damage and repair patterns found at the CAB are: (1) totally collapsed section C, (2) signs of repair in section C prior to the collapse (buttresses and trowel lines applied before the collapse), (3) the gaps of section B, D, and F, (3) major cracks in sections A, C, and E, cutting through the walls, (4) tufa deposits on the outside walls of sections A, C, and E, (5) curved (warped) trend of the bridge canal in section E, (6) damage to corners of pillars in section E, (7) broken canal and laterally shifted canal wall in section I, and (8) missing traces of the new canal other than in section G, (9) large wall-breakouts in section A and E. Further, a direct connection of the northern end of section A with the southern end of section E leads to a high gradient of 1.4%, as contrasted to the level of the canal in G with a gradient p. 0.35% (Fig. 11a).

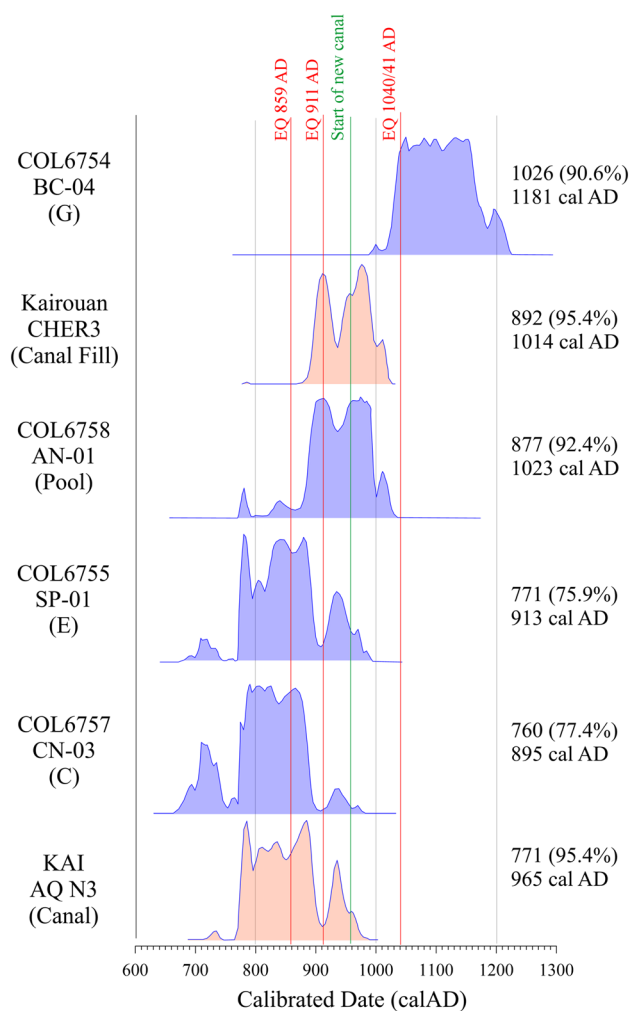


Fig. 12 Results of C14 radiocarbon dating of samples from the CAB. Name of sample and location of sampling (in brackets) is given on the left side and in Fig. 5b. The two red shaded curves are from Bahrouni et al. (2020a, 2020b) the blue shades one from this study. Dates on the right side give the 2σ uncertainty range; the historically documented time of three earthquakes (Ambraseys 2009; Kharrat et al. 2019; Bahrouni et al. 2020a, b) and the inferred start of construction of the new canal are indicated by red and green lines, respectively

4 Earthquake scenarios

In the following, we develop a model to estimate ground motions at the CAB and the Kairouan region to test the plausibility that local earthquake sources caused the observed damage at the bridge and correlate with the damage described in historic records. Synthetic seismograms are calculated with the Green's function method. The latter uses the elasto-dynamic representation theorem to construct ground-motion time histories (Aki and Richards 1980). Slip history of sub-sources distributed on the assumed activated fault sections is convolved with the Green's functions and integrated over the entire source; we use the approach by

Wang (1999) implemented in the computer codes QSgrn09 and QScmp09 (Wang 1999).

The Green's functions are calculated for selected fault sources and receiver positions based on a 1D subsurface model. Once the set of vertical, radial, tangential and pressure velocity Green's functions exists for the elementary source types strike-slip, dip-slip, and compensated linear vector dipole, earthquake scenarios can be constructed in which the earthquake source is defined by one or several fault segments which are activated during a given event. The segments are characterized by orientation and dimensions of the fault plane, and timing parameters including position, strike, dip and horizontal and vertical extension. The strength is controlled by the inferred seismic moment and the energy magnitude, and the rupture process is simulated by the activation of the sub-sources on the segment plane with respect to the chosen rupture velocity and direction(s) with which the circular rupture front expands; the rupture direction is controlled by the placement of an assumed hypocenter. The models used in the following do not include local site effects.

4.1 Subsurface model

The 1D velocity model (Fig. 13) for the calculation of the Green's functions is based on the CRUST1 model (Laske et al. 2013) for the grid cell 9.5°E/35.5°N (northern Tunisia). The depths of the layers at the Kairouan area were interpolated from the depths at the eastern and western edges of the grid cell for the location. The values of velocities and density were taken from the model. However, the densities of the middle and lower sediment layers were set to 1.60 and 1.70 Mg/m³, respectively, instead of the unrealistic low values in the CRUST 1 model of 0.97 and 1.27 Mg/m³. *Q*-values and the structure below the Moho discontinuity are based on PREM (Dziewonski and Anderson 1981).

4.2 Fault model and sources

The source model is based on the tectonic map resulting from field investigations of the Kairouan area as shown in Fig. 14. The algorithm used for the calculation of the synthetic seismograms requires fault sections with straight lines in the strike direction, and the potentially activated fault sections were idealized by the red lines given in Fig. 14. Five potential sources are considered: the El Qarn thrust fault is modeled with three scenarios. One comprises activation of the southwestern section (ELQ1), one with activation of the northeastern section (ELQ2) and a third scenario where both sections rupture during a single earthquake (ELQT). South of the CAB is the Qasr AlMa thrust fault (QAM). The other two scenarios are the strike-slip faults of Cherichira

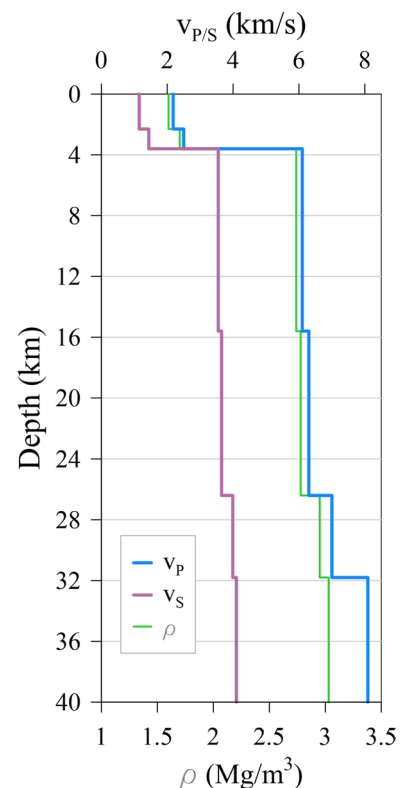


Fig. 13 1D velocity and density model for the Kairouan area

(CHE) and Cululis (CUL). Table 5 gives the parameters of the source segments.

For each of the six sources, three rupture scenarios were assumed, two with unilateral rupture spreading from opposite ends of the faults, and one bilateral spreading starting at the center of the fault segment(s). A constant rupture velocity of 2.80 km/s was used, which is about 80% of the S-wave velocity at the hypocenter region. Ruptures running from NW to SE (ELQ1, ELQ2, ELQT, CUL, QAM) and W–E (CHE) were labeled as mechanism 01, ruptures in the opposite direction as 02 and the bilateral model as 03; i.e., for mechanism 01 the rupture front approaches the CAB. Hypocenters were placed at 8 km depth and for the unilateral ruptures at a short distance from the edge of the fault plane, a stress drop of 1 MPa was assumed. All fault planes and hypocenter positions are shown in Fig. 14.

4.3 Synthetic seismograms

Acceleration, velocity, and displacement seismograms were calculated and plotted for the six earthquake scenarios with three rupture models each for the CAB and the Great Mosque of Kairouan. Figure 15 shows a summary of the three component velocity seismograms for the CAB for all 18 scenarios. All seismograms for all scenarios at the two

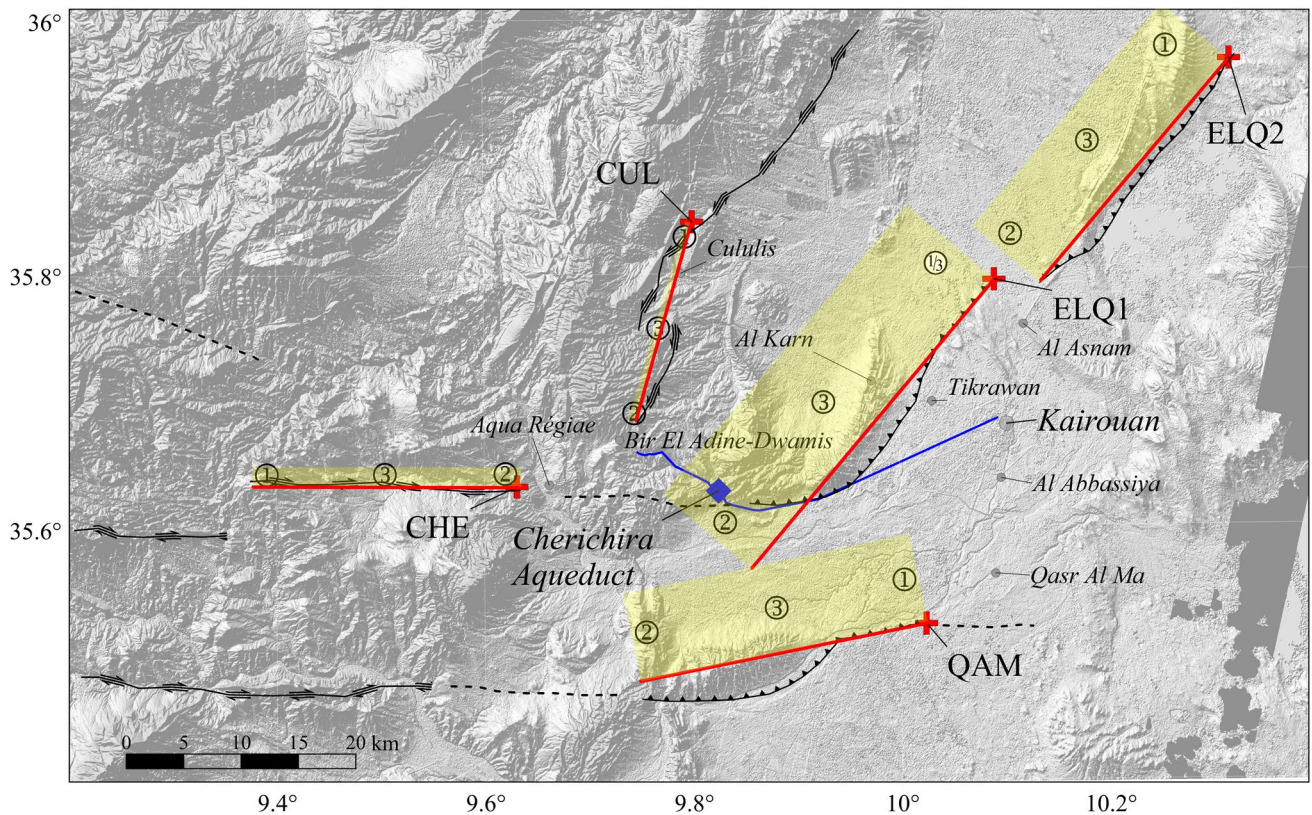


Fig. 14 Source model for the Kairouan area. Black lines show the major fault elements. Red lines are the surface traces of the rectangular fault segments. The red crosses show the reference points for the sources (Table 5) and the yellow shaded areas indicate the surface projection of the idealized fault planes. Black circles numbered 1, 2, and 3 indicate the epicenters for three rupture processes for each

source. Gray circles give location of villages possibly damaged by the earthquake scenario. The blue line indicates the trend of the Cherichira aqueduct (Army Map Service 1942) and the blue diamond the location of the CAB. The digital terrain model is from ALOS World 3D (Takaku et al. 2014)

Table 5 Parameters of the seismic sources model

Source	M_w	Reference Point		Strike deg	Dip deg	Rake deg	M_0 (Nm)	Length (km)	Width (km)
		Lat	Lon						
ELQ1	6.7	35.795	10.093	220	45	90	$1.41E+19$	33.0	14.0
ELQ2	6.5	35.967	10.322	220	45	90	$7.08E+18$	25.5	11.0
ELQT	7.2			220	45	90	$7.94E+19$	58.0	13.0
CUL	6.1	35.842	9.802	196	87	120	$1.78E+18$	18.0	8.0
CHE	6.3	35.635	9.632	270	79	105	$3.55E+18$	23.4	9.0
QAM	6.5	35.525	10.025	258	45	90	$7.08E+18$	25.5	11.0

sites (CAB and Kairouan) are shown in the electronic supplements (Fig. S2–S13).

As expected, large differences exist between the strength and duration of the ground motions at the CAB. Due to its rupture size and strength and close vicinity of the fault to the bridge, ELQT requires M_w 7.2 (Table 5) to cause the largest ground motions but also shows a strong directivity due to the rupture process as visible in Fig. 15. Rupture processes 01 and 03, where the rupture front approaches the CAB, causes larger peak ground velocities (reaching 1.5 m/s) than

during process 02 with the epicenter closer to the bridge. A rupture propagating away from the CAB results in a PGV of 0.5 m/s. The same is valid in principle for ELQ1 (which forms the southern section of ELQT), except the PGVs are smaller (maximum of 1.1 m/s) due to a smaller seismic moment. While the QAM source is also capable of producing a PGV just above 0.5 m/s, the ground motions from all other sources do not exceed 0.25 m/s.

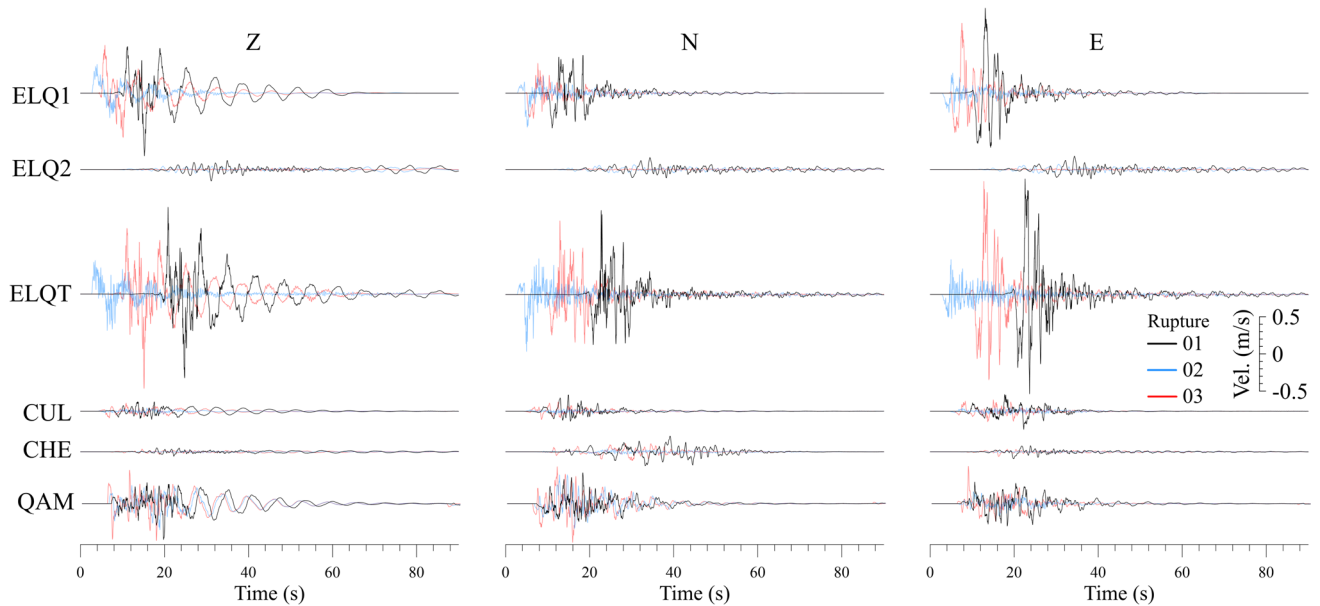


Fig. 15 Summary of velocity proportional ground motions at the CAB for all six sources which are labeled at the left of the seismograms. The left middle and right columns show the vertical (**Z**), north-south (**N**), and east-west (**E**) components of the ground

motions. The color of the seismogram traces indicates the rupture mechanism as given in the legend on the right; all seismograms are plotted to the same scale which is also shown on the right

4.4 Ground motion parameters and intensities

The RMS (root mean square) values of the peak ground velocity (PGV) and peak ground acceleration (PGA) of the two horizontal components were determined from all synthetic seismograms and are plotted with respect to each other in Fig. 16. In addition to these ground-motion parameters, the figure shows Modified Mercalli intensity (MMI) ranges as suggested by Wald et al. (1999), the same scheme as used in USGS *shake maps* (Worden et al. 2020). This allows a rough estimate of the intensities at three sites, the CAB, the Great Mosque of Kairouan, and the center of the old city of Soussse.

Additionally, for each of the 18 earthquake scenarios, response maps were calculated for 5% damping at selected frequencies. From the response values at zero frequency, the distributions of RMS values of PGA and PGV of both horizontal components were determined. By applying the above-mentioned scheme suggested by Wald et al. (1999), the distribution of MM intensities was calculated. As an example, Fig. 17 shows the maps for the three ELQ1 scenarios. (Intensity maps of all scenarios are shown in the electronic supplements (Figs. S14–S19).

5 Flash flood

An important part of quantitative archaeoseismological studies is the comprehensive consideration of alternative causes of damage found at archaeological sites (Galadini

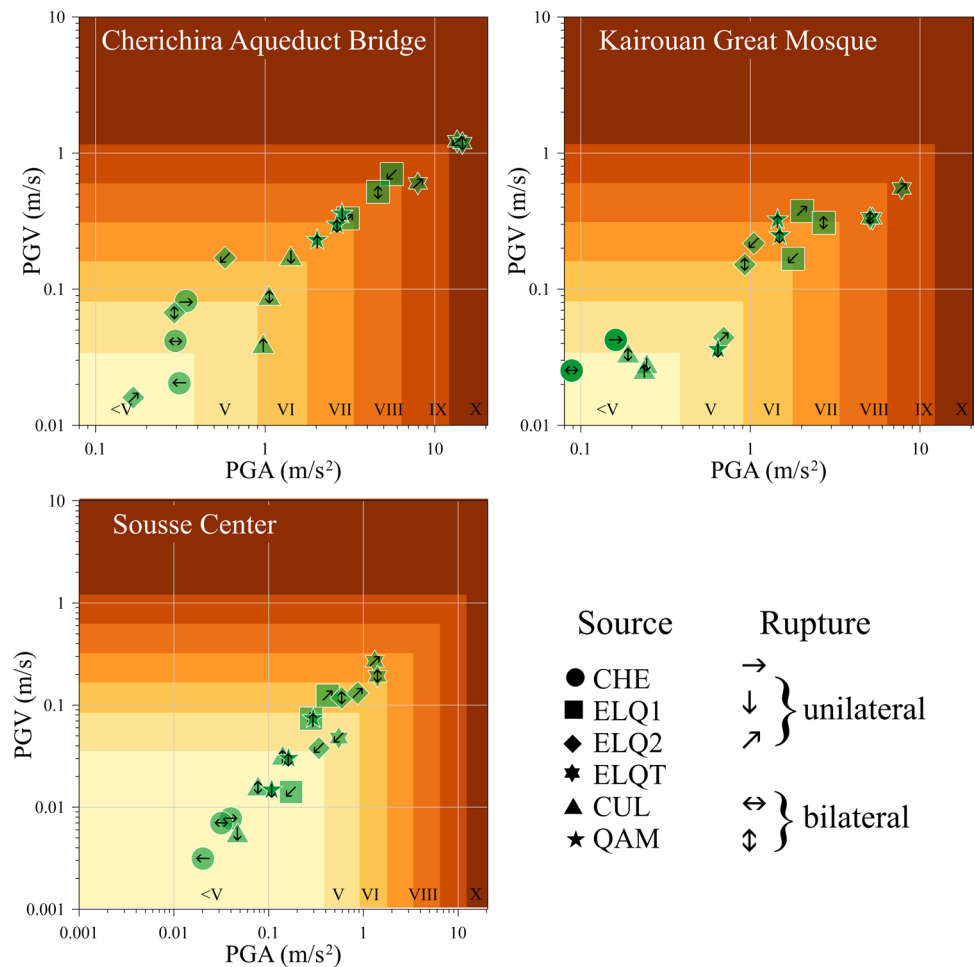
et al. 2006; Hinzen et al. 2009). As mentioned above, the pillars of the CAB in section C show severe damage at the corners in the lower ± 3 m. Because the corners, made from worked ashlar some reaching $0.6 \times 0.5 \times 0.3$ m³, are attractive secondary building material, it cannot be excluded that the corner stones were at some point in time robbed up to a height reachable from the current ground level. However, it should be noted that this is also the height range most vulnerable to flash floods in the wadi.

The Cherichira area west of Kairouan has a semi-arid Mediterranean climate. Also, typical are seasonal rainfalls which can cause flash flooding in Oued el Mouta, and could have constituted a threat to the structural integrity of the CAB.

For a rough estimate of the possible flood discharge through the bridge, we assume a heavy rainstorm with 200 mm of rain dumped in half an hour. Local witnesses report that such storms with strong rainfalls have previously been observed in Kairouan and Tunisia regions (<https://www.france24.com/en/20180924-tunisia-weather-cap-bon-record-rains-set-off-deadly-flash-floods-nabeul>, last accessed Jan 2021). Figure 18 shows the terrain model of the Cherichira area (see data and resource) and an overlay with the result of a watershed analysis implemented with SURFER (Golden software) using a cell threshold of 12,000. The size of the basin which drains into the Oued Mouta is close to 20 km².

With the assumed 200 mm (0.2 m) of rain on 20 km², the total rain volume is 4×10^6 m³. Assuming further a runoff

Fig. 16 RMS values of the peak ground (PGV) velocity of the two horizontal components plotted in relation to RMS values of the peak ground acceleration (PGA) from synthetic seismograms for six source models; the left, middle, and right graphs show values for the CAB, the location of the Great Mosque in Kairouan, and the center of the old city of Sousse, respectively. The symbol type indicates the source as shown in Fig. 14. Arrows within the symbols indicate the rupture direction, unilateral or bilateral, as shown in the legend. Roman numerals in the color-shaded areas give the range of MM intensities following the model of Wald et al. (1999). The lower intensity scale in the bottom graph for the Sousse Center



of 20% total rain volume, the water crossing the bridge is $800,000 \text{ m}^3$ in 30 min equivalent to $444 \text{ m}^3/s$.

Using again the formulation by Gauckler–Manning–Strickler, now with parameters for a trapezoid river bed that has growing bushes and trees ($k_{sr} = 17.5 \text{ m}^{1/3}/s$) and taking the full crosscut ($A = 140 \text{ m}^2$, Fig. 18), the runoff is $485 \text{ m}^3/s$ with a velocity of 3.5 m/s. If the cross-cut is reduced to the gap between the pillars ($A = 28 \text{ m}^2$), the runoff is reduced to $142 \text{ m}^3/s$ and velocity increased to 5.1 m/s. This means it would take about 90 min to drain the accumulated water behind the barrier formed by the bridge. Such a stream of water could well explain the damaged corners of the pillars reaching on average a height of 3.4 m (Table 2). In actuality, local eyewitnesses questioned during the field campaign reported seeing flooding, which ‘almost reached the top of the arches’ of the CAB.

6 Discussion

The analysis of the CAB for possible earthquake damage required reconstructing the history of the aqueduct through the Roman, Aghlabid and Fatimid periods until its ultimate abandonment. Our measurements taken from the scan of the CAB are in accordance with the interpretations of Mahfoudh et al. (2004) and Gauckler (1900) that the massive base of the bridge with the four arches and pillars is of Roman origin based on the pillars corresponding to the Roman proportion (Table 2). On top of this, almost 3-m-wide basis is a 1.5-m-wide wall that supports the Aghlabid water canal. The contact between the Roman and Aghlabid sections is rather irregular, and it seems clear that during the retrofitting of the Roman

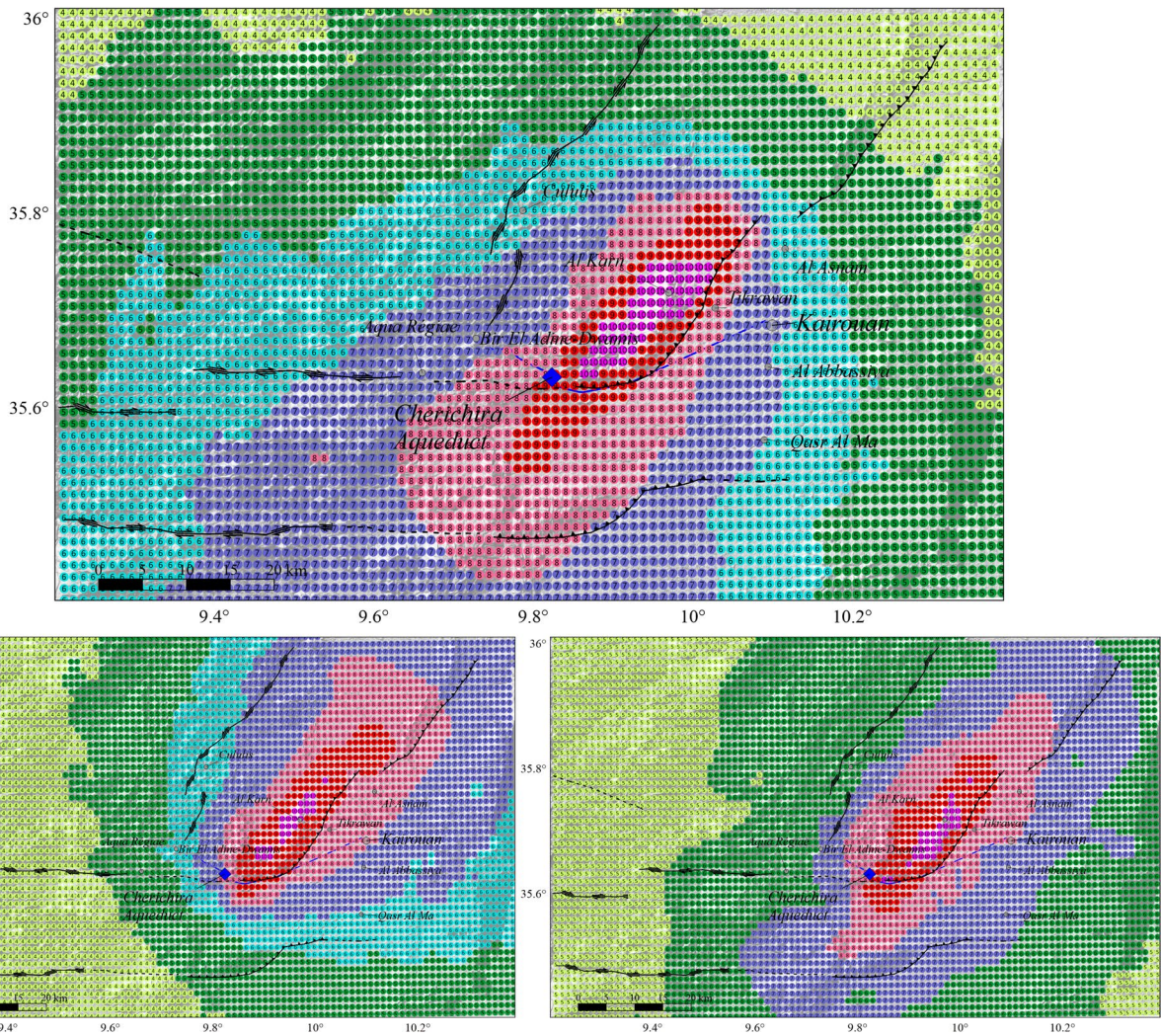


Fig. 17 Numbers in the colored dots give the MM intensities based on PGA and PGV values for the horizontal components for the ELQ1 scenario. The top shows the result for rupture mechanism 01, bottom left and right for the mechanisms 02 and 03, respectively

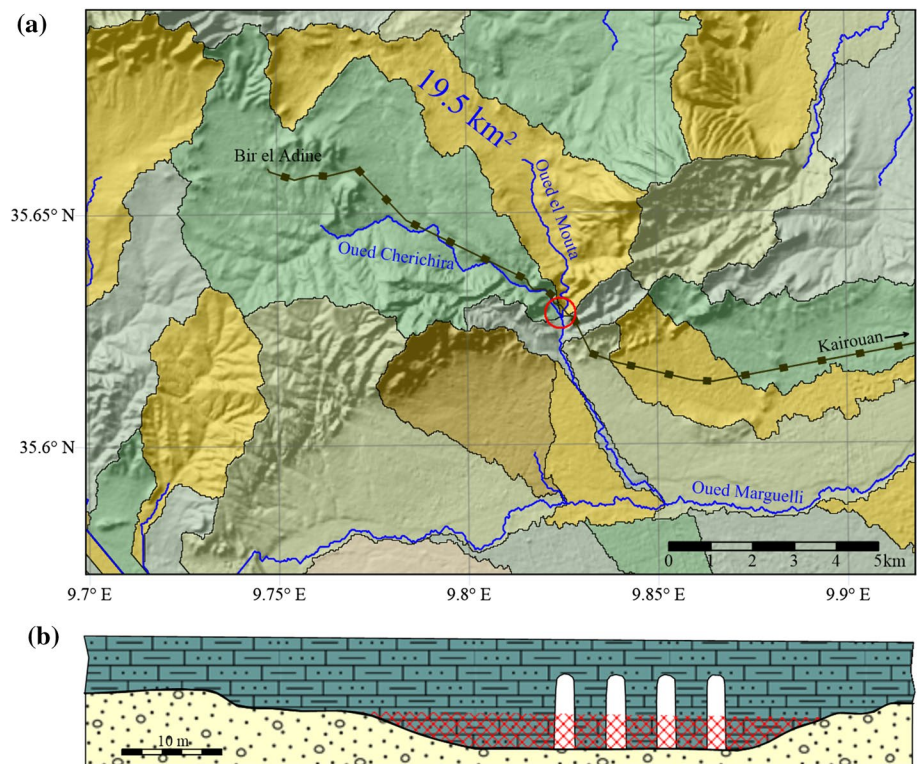
bridge the Aghlabid builders used as much of the Roman construction as possible. Spolia in the form of large blocks (Fig. 8c) and ruins from a former water canal, probably of Roman origin, indicate that such material must have been still existing in the vicinity of the structure in the ninth century AD when the aqueduct was retrofitted, also a sign of the decay or destruction of the original Roman bridge; however, this earlier deterioration process is outside the scope of this study.

While Baklouti (2021) in a recent paper doubts that an Aghlabid building phase of the CAB exists, the previous and new C¹⁴ dates confirm that the first retrofitting occurred during the Aghlabid period (AD 800–909). The much larger dimension of the canal in section G and its 1-m-higher elevation as compared with the Aghlabid canal is a clear sign that this is part of a later construction. This conclusion is supported by the historic report that in AD 959 the Fatimid

once more retrofitted the bridge (Halm 1996). In addition, Mahfoudh et al. (2004) report that the new larger canal even blocked and replaced the former, which agrees with the cement and stone fill we found in section C.

The origin of the gaps of sections B, D, and F is not unambiguously resolved. However, as the site is poorly protected, there are many traces of re-used stone masonry material from the CAB in structures in the surrounding buildings showing that easily reachable and transportable materials have been removed from the site over a millennium. At the southern end of section A, a dirt track crosses the trend of the bridge and all stones are gone (Fig. 3a). South of this path much debris from the aqueduct is still visible, but not accessible as it is overgrown. The gap in section D also intersects a path and is in the lowest part of the wadi, so both anthropogenic removal of material, burial under alluvial and colluvial deposits, and hydraulic action can posit as causes

Fig. 18 **a** Terrain model of the Cherichira area west of Kairouan overlain with the result of a watershed analysis with rivers in blue and color-shaded basins with black border lines. The trend of the Cherichira aqueduct is shown by the line with square dots. The red circle marks the location of the CAB at the junction of the Oued Cherichira and the Oued Mouta. Further indicated is the surface size of the basin draining into the Oued Mouta. **b** Simplified crosscut at the CAB. The contour of the river bed follows the terrain model in Fig. 4a; the red-hatched section ($h=3.5$ m) of the river bed comprises a crosscut area of 140 m^2



for the gap. Although bridge pillars are still standing, no clear explanation exists as to why the 18-m-long section between E and G has disappeared. The problem of the non-existent remains of the Fatimid canal in section E while the ruin of section I is still in place is also unresolved.

The tufa spills (particularly those in section E) are a clear indicator that the bridge from section A to E must have been intact when water spilled in heavy streams down the walls of the bridge (Fig. 10); for the case of an interrupted canal, the water would not have reached all spill sections. On the other hand, even at the major cracks cutting through and displacing parts of section I (Fig. 10), no tufa deposits are present, which means that the structural damage here occurred when no significant water flow existed in section I. Either (1) the damage in the upstream parts where the deposits exist was so large that water failed to reach section H and I, or (2) the structural damage in section I occurred at a later time, possibly coinciding with the collapse of section C. If the coincidence was true, a flash flood would be an unlikely cause for the collapse of section C as the streaming water would not have reached section I.

A further argument for a seismogenic cause of the cracks is their morphology. The cracks start from the top of the bridge and propagate downwards almost vertically (in section E reaching a length of up to 4.5 m; Fig. 10); however, they do not reach the base of the bridge. This excludes a genesis through quasi-static settlement but could be explained by an increasing amplitude of a lateral (off-plane) wavy

motion and shaking of the bridge from bottom to top, a hypothesis that could be tested with a dynamic model of the bridge.

To shed more light on the fate of the CAB, the observations, measurement results, and historic reports have to be sorted according to approximate dates. Figure 19 shows a timeline with results of C^{14} dating, historic events and data from the earthquake catalogs. Due to the relative short time span during which the (repeated) damage and repair intervals of the CAB and the uncertainty in the physical dating (Figs. 12 and 19), a clear temporal delamination of the events is not presently possible. However, the radiocarbon dating brackets a few events. With high probability, the canal section south of the bridge (Bahrouni et al. 2020b) was built contemporaneous with the canal of section C and the wall in section E during the Aghlabid period and before the earthquake of AD 859. The small pool, a few hundred meters upstream from the bridge (Fig. 4b), can be assumed to be contemporary with the initial filling of the canal south of the bridge as the two-sigma ranges of the samples from each correlate: AD 892–1014 and AD 877–1023, respectively. It can be reasoned that after a damaging event, the CAB was dysfunctional, and the canal south of the bridge started to fill with sediment, but the water flow in the section north of the bridge was still working. The pool was then constructed to collect and distribute water locally, e.g. as a cattle watering tank. The uncertainty in the dating prevents discrimination between the AD 859 and the AD 911 earthquake or both as

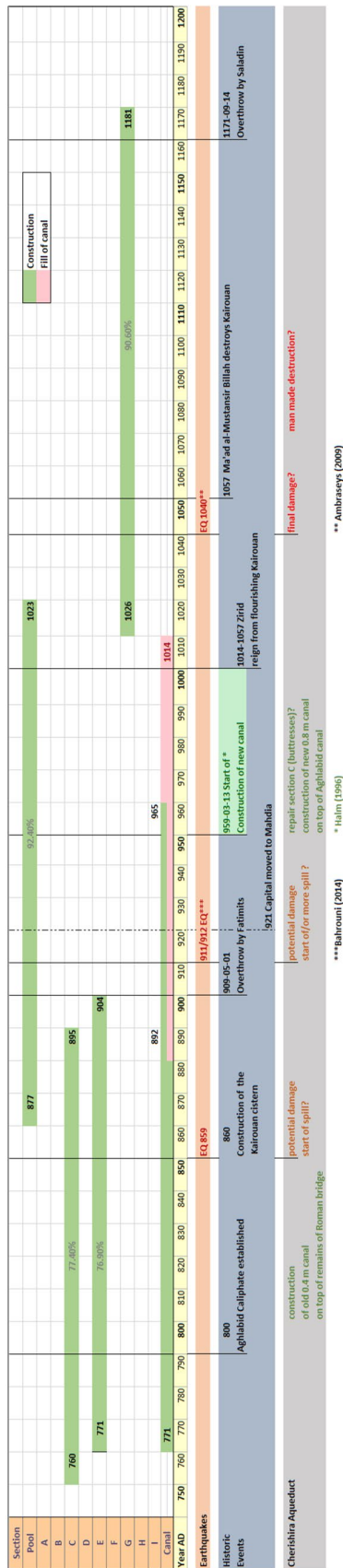


Fig. 19 Timeline of the sequence of events at the CAB from 8th to 12th century AD. Green and pink shaded lines indicate the 2-sigma intervals of C¹⁴ dating in sections of the CAB given on the left. Further indicates is the time of three earthquakes (red shading) and historic events in the blue shaded row. At the bottom (gray) events at the CAB are indicated

the damaging event(s). However, the damage reported from the villages in the Kairouan area, in Kairouan itself and in Sousse make the AD 859 earthquake a favored candidate (Bahrouni et al. 2020b). This is supported by the construction of a large round 130 m diameter and 5 m deep water basin in AD 860 as a countermeasure to water shortage in Kairouan, probably because of the interruption of the aqueduct (Bahrouni et al. 2020b and references therein). If this event triggered the spill, there would have been a 100-year period before the historically documented construction of the new Fatimid bridge canal which started on March 13 in AD 959 (Halm 1996), and the repairs in section C including the buttresses might have been necessary to support the new Fatimid bridge canal.

Inconsistent with this historically documented date of the canal construction is the age of the sample from section G which is the youngest, but the beginning of the two-sigma range (AD 1026–1181) is more than 100 years later than the historically documented start of the construction of the Fatimid canal (Halm 1996). Further radiocarbon dating is necessary to clarify between building/damage hypotheses.

The hypothesis by Bahrouni et al. (2014) that the AD 911/912 earthquake caused the (final) destruction of the aqueduct can be disregarded because the Fatimid canal dates later. If an earthquake caused the final destruction of the bridge, the event of 1040/41 (Ambraseys 2009) is a possibility that agrees with all historic and physical dates available at this point.

Our rough estimate of the damaging potential of a flash flood in the Oued el Mouta (under the CAB) and eyewitness reports about recent floods, which were even larger than the one we assumed, show that a high water level and related flow rate may well have harmed the integrity of the CAB during its long history. The heavily damaged corners of the lower part of the pillars look more like the consequence of streaming water than ground motion from earthquakes, e.g. the consistent height of the damaged section could well be explained by horseshoe vortexes in the currents between the pillars. However, the cause of the total collapse of section C and the gap of section D are still unresolved. When the water flow of a stream is forced through a narrowing, e.g. a bridge, scouring effects occur, the severity of which depend on the strength of the water flow and the soil conditions along the embankment (Arneson et al. 2012). Particularly during sudden flooding events, flow concentration and boundary interactions lead to turbulence which in turn can cause scour destabilization of the channel bank. A contributing factor in flash floods can also be floating debris (tree stems, etc.) partially blocking the passage. A possible scenario at the CAB would be a washout of the embankment north of pillar 1 and eventually a slope failure causing the collapse of the abutment in section C. Arneson et al. (2012) also point out, that repeated floods cause accumulating effects and the

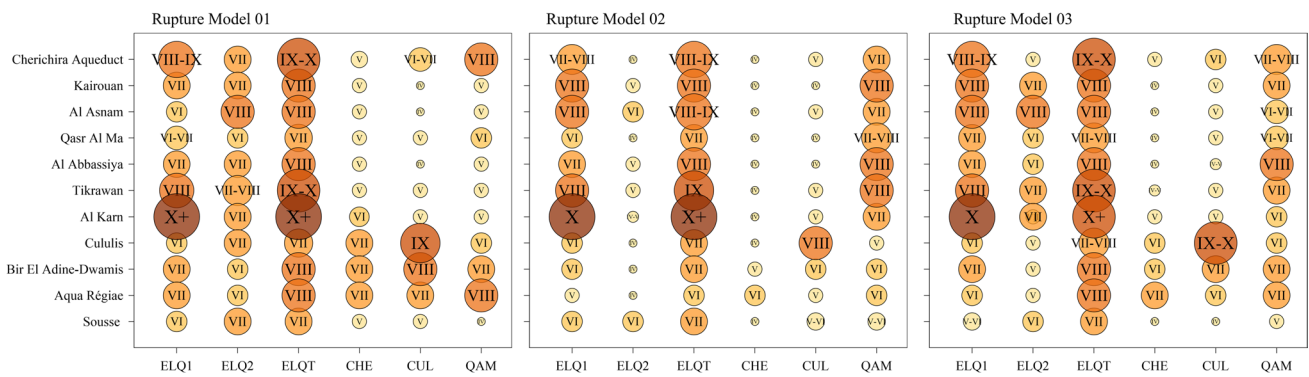


Fig. 20 Summary of the estimated MM intensities for 11 sites (names on the left axis) and the 18 earthquake scenarios; the rupture models and the related directivity are given above the graphs and as in Fig. 16; circle size scales with the intensities given in Roman numerals

scour depth can increase from event to event. However, flash flooding alone cannot explain the cracks and ruptures on the bridge, particularly those in section I. Further excavations in section C combined with model calculations are required to clarify a hypothesis that a flash flood and scour destabilization (or a local landslide) caused irreparable damage to the CAB in section C.

On the other hand, if the damage to the CAB during the different phases is coseismic, this requires estimation of earthquake intensity large enough to account for the damage and ultimately partial destruction of the CAB. Figure 20 summarizes the results of the intensity estimates for the CAB, the cities of Kairouan and Sousse and villages which suffered damage during the AD 859 earthquake for the six sources and three rupture mechanisms of our model. The method we used to translate PGV-PGA combinations to macroseismic intensities was calibrated by Wald et al. (1999) for MMI.

Historic reports name sites (Fig. 14) that suffered damage during the AD 859 earthquake (Bahrouni et al. 2020b and references therein). Following Musson et al. (2009), it seems feasible to assume the intensity grades of MMI are similar to those of the EMS-98 scale (Grünthal 1998) and to be severe enough to be reported, this indicates structures suffered a minimum of damage grade 3–4 of the EMS-98 scale. Even considering a high vulnerability of rural structures in the villages, vulnerability class A-B of the EMS-98 scale (Grünthal 1998), intensity can be surmised to be at least VI–VII. Our model predicts that CUL and CHE sources would not meet the criteria. Depending on the rupture model, these sources result in 7–10 out of the 11 locations with intensities V or less. Rupture models 02 and 03 for ELQ2 can also be excluded for the same reason. Mechanism 01 for ELQ2 causes intensities of VI at three sites, and is even higher at the other locations (Fig. 20). For the QAM, source mechanism 01 results in six locations with intensity V or less. For the other two mechanisms, only one location results in such

low shaking levels; however, for mechanism 03 this location is Sousse. If the damage in Cululis was as severe as suggested (Bahrouni et al. 2020b), then only the CUL source could have resulted in intensity IX–X at Cululis; the other scenarios produced intensity VII–VIII or less.

At the CAB, the scenario ELQ1/01 and ELQ1/03 produce intensity VIII–IX due to the directivity effect; scenario ELQ1/02 results in intensity VII–VIII as the rupture propagates away from the bridge (Figs. 14 and 20). Due to the larger distance, the intensities for ELQ2 are lower for all three mechanisms (VII, < V, and V, respectively). On the other hand, the three rupture mechanisms of source ELQT produce intensity IX–X, VIII–IX, and IX–X at the bridge site where IX–X might be too high for the first damaging event but feasible for the final destruction. Paleoseismic investigations along the ELQT fault segments may provide a better estimate of seismic parameters and size of past earthquakes.

Among the strike-slip fault scenarios, only CUL/01 produces an intensity above VI at CAB but could not account for damage in Kairouan. Whether the ground motions corresponding to intensity VI–VII would be sufficient to explain the observed damage (e.g. spill cracks or section C bridge collapse) is one of the goals of planned future testing with a DEM of the CAB.

Most but not all observations of damage at the CAB can be related to earthquake ground motions. Figure 21 summarizes the plausibility of observed damage and potential cause for the CAB in the form a matrix (Galadini et al. 2006; Hinzen et al. 2012) categorizing the damage/cause relation simply feasible, questionable, or unfeasible. Plausibility is then quantified by a number between 0 and 1 (Hinzen et al. 2012), meaning that none or all of the observations can be explained by a particular cause, respectively. Six causes are linked to 11 observations which have been discussed above with the highest score of 63% possibility assigned to a seismogenic origin.

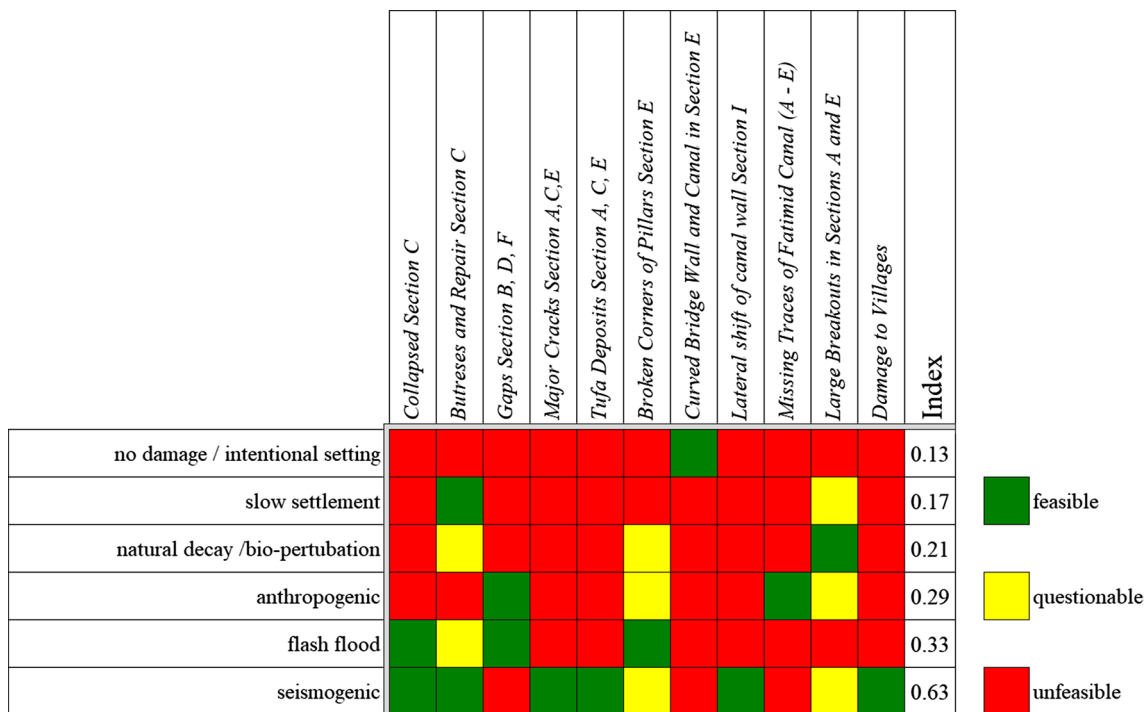


Fig. 21 Plausibility matrix linking six potential causes of damage (rows) with 11 observations or damage descriptions of the CAB and its surrounding. The index is a measure of plausibility of a single cause in terms of all observations and damage descriptions (Hinzen et al. 2012)

7 Conclusion

The CAB was an essential and neuralgic part of the Cherichira aqueduct, an important freshwater supply to Kairouan holy city. The shaking, damage and partial destruction of such a massive bridge required significant energy. Originating in Roman times, it must have undergone a long period of degradation and damage (of still unknown origin) either during or after the Roman era ended before its first retrofitting during the Aghlabid period (AD 800–903). Considering the radiocarbon ages of different sections of the bridge and the canal up- and downstream, there is a high probability that the AD 859 earthquake damaged the CAB so severely that the aqueduct no longer functioned, and water started to spill through cracks that likely were of a seismogenic origin. Later, the canal downstream filled with sediments. It is less likely, though not impossible, that the cracks formed (or increased) during the AD 911 earthquake. In AD 959, the retrofit of the bridge and the construction of the larger Fatimid canal began, and it is less likely that 48 years of spill were sufficient to deposit the (still existing) tufa at the sides of the CAB. In case of damage during the AD 859 earthquake, there would have been a potential 100-year spill period. The radiocarbon age of the sample from section G of the Fatimid canal is the youngest; however, it is too young to be compatible with the historic date of the Fatimid retrofitting. More dating samples are required to

better constrain the sequence of events. The AD 1040/41 earthquake reported by Ambraseys (2009), is a potential candidate for the final destruction of the CAB with the total collapse of section C. However, it cannot presently be ruled out that the (repeated) action of flash floods in the wadi el Mouta contributed to the final bridge collapse. Even though we used only a deterministic approach, our model of the ground motions of potential local earthquake sources shows that earthquakes at the El Quarn fault or the Qasr AIMa of M_w 6.7 and 6.5, respectively, can have produced the macroseismic intensities necessary to cause the described damage at the CAB and the villages in the surrounding area. We intend to further the study in two ways; (1) paleoseismic investigations along faults to provide seismic parameters of past earthquakes, along the ELQ fault segment in particular, and (2) to construct a 3D discrete element model of the CAB to test its dynamic behavior and to quantify the earthquake mechanics necessary to cause the damage. Additionally, the model can be used to further explore the possibility of a hydraulic cause.

The CAB is located in the Cherichira natural park and thus further looting should be prohibited, but natural forces (rain, floods) can further reduce its integrity. The laser scan of the CAB shows that the bridge is in some parts in a delicate state and the existing damage might lead to further degradation of this important piece of cultural heritage. For example, parts at the base of the western wall in section

A have fallen out so that the original width of the wall is reduced from 1.4 m to just 0.7 m over a stretch of several meters. At the base of the western side of the substructure in section E, a large chunk of more than 6 m³ volume of the wall is missing that threatens the stability of the wall over a stretch of ~7 m. Also, severe is the damage of the pillars in section E. Here, erosion at the base of pillar 3 has reduced its crosscut surface from 8.6 to just 4.2 m². At the northern face of pillar 1, a through-going crack has separated a large block of more than 13 m³ with an estimated weight of 37 t, which would be a threat when falling down the 9.5 m. Mitigating further decay of the Cherichira aqueduct bridge and its classification as a protected archeological site in Tunisia should have a high priority.

Supplementary Information The online version contains supplementary material available at <https://doi.org/10.1007/s42990-021-00062-9>.

Acknowledgements We thank L. Garsellaoui, the manager of Cherichira National Park, for the permission and support and the director general of the National Heritage Institute of Tunisia, F. M. Forthe for the work at the Cherichira aqueduct. During the field campaigns at Cherichira ONM, engineers M. Arfaoui and A. Oueslati helped with data acquisition for the laser scanning and collecting dating samples. The National Institute of Meteorology of Tunisia provided the seismic equipment and helped acquire the ambient noise data. We thank the team of Cologne AMS, particularly J. Rethemeyer and B. Bock for the radiocarbon dating. We are grateful to R. Wang for providing his computer codes for the calculation of Green's functions and synthetic seismograms and the very helpful discussions with him about the application of the method. We thank Fabrizio Galadini and an unknown reviewer for very helpful comments and editor Attila Çiner for handling the manuscript.

Funding Open Access funding enabled and organized by Projekt DEAL. Financial support for the field investigations came from l'Office National des Mines of Tunisia, from Institut National des Sciences de l'Univers (INSU, France) for radiocarbon dating.

Declarations

Conflict of interest The authors declare that they have no conflict of interest.

Resources Maps in Figs. 2, 13, and 15 are based on services provided by the OpenTopography Facility with support from the National Science Foundation under NSF Award Numbers 1833703, 1833643, and 1833632 (<https://opentopography.org/>, last accessed Dez. 2020). Five Charcoal samples were dated at CologneAMS (<https://cologneams.uni-koeln.de/> last accessed May 2021), two samples were processed by Beta Analytic (Florida, <https://www.radiocarbon.com/>, last accessed May 2021). Information from <https://www.gabriel-strommer.at/en/calculators/flow-velocity-flow-rate/>, (last accessed Feb. 2021) was used to estimate flow rates. Figures unless stated differently were prepared with Grapher and Surfer, Golden Software (<https://www.goldensoft.com/>, last accessed May 2021). Synthetic seismograms were calculated with programs qsgn09 and qscmp09 (<https://www.gfz-potsdam.de/en/section/physics-of-earthquakes-and-volcanoes/infrastructure/tool-development-lab/>, last accessed Dez. 2020).

Open Access This article is licensed under a Creative Commons Attribution 4.0 International License, which permits use, sharing, adaptation, distribution and reproduction in any medium or format, as long as you give appropriate credit to the original author(s) and the source, provide a link to the Creative Commons licence, and indicate if changes were made. The images or other third party material in this article are included in the article's Creative Commons licence, unless indicated otherwise in a credit line to the material. If material is not included in the article's Creative Commons licence and your intended use is not permitted by statutory regulation or exceeds the permitted use, you will need to obtain permission directly from the copyright holder. To view a copy of this licence, visit <http://creativecommons.org/licenses/by/4.0/>.

References

- Aki K, Richards PG (1980) Quantitative Seismology Theory and Methods, Vols. I and II, W. H. Freeman, San Francisco, California
- Albini P, Musson RMW, Gomez Capera AA, Locati M, Rovida A, Stucchi M, Viganò D (2013) Global historical earthquake archive and catalogue (1000–1903), GEM Technical Report 2013-01 V1.0.0, 202pp. GEM Foundation, Pavia. <https://doi.org/10.13117/GEM.GEGD.TR2013.01>
- Ambraseys NN (2009) Earthquakes in the Mediterranean and Middle East: A Multidisciplinary Study of Seismicity up to 1900. Cambridge University Press, Cambridge, p 947
- Army Map Service (1942) Map Tunisia 1:50,000, Kairouan sheet 63. US Army
- Arneson LA, Zevenbergen LW, Lagasse PF, Cloppe PE (2012) Evaluating scour at bridges. U.S. Department of Transportation Federal Highway Administration Report No. FHWA-HIF-12-003HEC-18. <https://www.fhwa.dot.gov/engineering/hydraulics/pubs/hif12003.pdf>
- Bahrouni N, Bouaziz S, Soumaya A, Ben Ayed N, Attafi K, Houla Y, El Ghali A, Rebai N (2014) Neotectonic and seismotectonic investigation of seismically active regions in Tunisia: a multidisciplinary approach. *J Seismol*. <https://doi.org/10.1007/s10950-013-9395-y>
- Bahrouni N, Masson F, Meghraoui M et al (2020a) Active Tectonics and GPS data analysis of the Maghrebian Thrust Belt and Africa-Eurasia plate convergence in Tunisia. *Tectonophysics*. <https://doi.org/10.1016/j.tecto.2020.228440>
- Bahrouni N, Meghraoui M, Hinzen K-G, Arfaoui M, Mahfoud F (2020b) The damaging earthquake of 9 october 859 in Kairouan (Tunisia): evidence from historical and archeoseismological investigations. *Seismol Res Lett* 91:1890–1900. <https://doi.org/10.1785/0220190258>
- Baklouti H (2021) Les installations hydrauliques antiques de Tunisie dans les sources arabes. *Étude Historiographique' Africa* 24:39–67
- Benjelloun Y, de Sigoyer J, Carlut J, Hubert-Ferrari A, Dessales H, Pamir H, Karabacak V (2015) Characterization of building materials from the aqueduct of Antioch-on-the-Orontes (Turkey). *CR Geosci* 347:170–180. <https://doi.org/10.1016/j.crte.2014.12.002>
- Brent SD (1984) Water and society in the ancient Maghrib: technology, property and development. *Antiq Afr* 20:121–173. <https://doi.org/10.3406/antaf.1984.1103>
- Chow VT (1959) Open-channel hydraulics. McGraw-Hill, New York
- Davis CA, O'Rourke TD (2011) ShakeOut scenario: water system impacts from a M7.8 San Andreas earthquake. *Earthq Spectra* 27:459–476
- Dziewonski AM, Anderson DL (1981) Preliminary reference earth model. *Phys Earth Planet* 24:297–356

- Eidinger J, de Castro L, Ma D (2006) The 1906 earthquake impacts on the San Francisco and Santa Clara water systems - What we learned, and what we are doing about it. *Earthq Spectra* 22:113–134. <https://doi.org/10.1193/1.2186986>
- El Ghali A, Bobier C, Ben Ayed N (2003) Rôle du système de faille E-W dans l'évolution géodynamique de l'avant-pays de la chaîne alpine de Tunisie. Exemple de l'accident de Sbiba-Chérichira en Tunisie centrale. *Bull Soc Geol Fr* 174:373–381
- Fréchet J, Meghraoui M, Stucchi M (2008) Historical seismology, interdisciplinary studies of past and recent earthquakes. Springer, Dordrecht
- Galadini F, Colini L, Giaccio B, Messina P, Slavi S, Sposato A (2003) Persisting effects of the Colfiorito (central Italy) Pleistocene paleo-landslide in the planning of land use: Upper Palaeolithic and proto-historical coexistence and Antique-Modern modifications. *Environ Geol* 43:621–634. <https://doi.org/10.1007/s00254-002-0665-1>
- Galadini F, Hinzen K-G, Stiros S (2006) Archaeoseismology: methodological issues and procedure. *J Seismol* 10:395–414. <https://doi.org/10.1007/s10950-006-9027-x>
- Galli PAC, Giocoli A, Naso JA, Piscitelli S, Rizzo E, Capini ST, Scaroina L (2010) Faulting of the Roman aqueduct of Venafrum (southern Italy): Methods of investigation, results, and seismotectonic implications. In: Sintubin M, Stewart IS, Niemi TM, Altunel E (eds) *Ancient Earthquakes*. Geological Society of America, Boulder, p 471. <https://doi.org/10.1130/SPE471>
- Garbrecht G (1986) Planung, Bemessung und Bau römischer Wasserversorgungsanlagen. *Atlas der römischen Wasserleitungen nach Köln*. Grewe K Rheinland-Verlag GmbH, Köln, pp 215–224
- Gauckler, P (1900) Enquête sur les installations hydrauliques romaines en Tunisie, Tunis, imprimerie rapide. IV:277
- Grewe K (1986) *Atlas der römischen Wasserleitungen nach Köln*. Rheinland-Verlag GmbH, Köln
- Grünthal G (1998) European Macroseismic Scale 1998 (EMS-98) Cahiers du Centre Européen de Géodynamique et de Séismologie 15. Centre Européen de Géodynamique et de Séismologie, Luxembourg
- Guidoboni E, Comastri A, Traina G (1994) Catalogue of ancient earthquakes in the Mediterranean Area up to the 10th Century. ING Roma-SGA, Bologna
- Halm H (1996) The empire of the Mahdi the rise of the Fatimids. *Handbook of oriental studies/Handbuch der Orientalistik* 26, Brill Deutschland GmbH
- Hinzen K-G, Fleischer C, Reamer SK, Schreiber St, Schütte S, Yerli B (2009) Quantitative methods in archaeoseismology, in: R. Pérez-López, C. Grützner, J. Lario, K. Reicherter, and P.G. Silva (eds) *Archaeoseismology and Palaeoseismology in the Alpine-Himalayan Collisional Zone*, Baelo Claudia, Cadiz Spain 50–51
- Hinzen K-G, Schreiber S, Fleischer C, Reamer SK, Wiosna I (2012) Archaeoseismic study of damage in Roman and Medieval structures in the center of Cologne, Germany. *J Seismol* 17:399–424
- Hinzen K-G, Maran J, Hinojosa-Prieto H, Damm-Meinhardt U, Reamer SK, Tzislakis J, Kemna K, Schweppe G, Fleischer C, Demakopoulou K (2018) Reassessing the mycenaean earthquake hypothesis: results of the HERACLES project from Tiryns and Midea, Greece. *Bull Seismol Soc Am* 108:1046–1070. <https://doi.org/10.1785/0120170348>
- Hoffmann G, Kummer S, Márquez R et al (2019) The Roman Eifel Aqueduct: archaeoseismological evidence for neotectonic movement at the transition of the Eifel to the Lower Rhine Embayment. *Int J Earth Sci (geol Rundsch)* 108:2349–2360. <https://doi.org/10.1007/s00531-019-01766-y>
- Kharrat S, Harbi A, Meghraoui M, Bouaziz S (2019) The Tunisian homogenized macroseismic database (second century–1981): first investigations. *Seismol Res Lett* 90:347–357. <https://doi.org/10.1785/0220180237>
- Ksentini A, Bouden-Romdhane N (2013) Updated Seismic Hazard Assessment of Tunisia. *Bull Earthq Eng*. <https://doi.org/10.1007/s10518-013-9548-y>
- Laske G, Masters G, Ma Z, Pasyanos M (2013) Update on CRUST10 - A 1-degree Global Model of Earth's Crust. *Geophys Res Abstracts* 15:2658 (**Abstract EGU2013-2658**)
- Lunedei E, Malischewsky P (2015) A Review and Some New Issues on the Theory of the H/V Technique for Ambient Vibrations. In: Ansal A (ed) *Perspectives on European Earthquake Engineering and Seismology*. Geotechnical, Geological and Earthquake Engineering 39. Springer, Cham. https://doi.org/10.1007/978-3-319-16964-4_15
- Mahfoudh F, Baccouch S, Yazidi B (2004) L'histoire de l'eau et des installations hydrauliques dans le bassin de Kairouan. Tunis. <http://www.edusfax.com/sfaxreader/french/2005Mahfoudh.pdf>
- Marco S (2008) Recognition of earthquake-related damage in archaeological sites: examples from the Dead Sea fault zone. *Tectonophysics* 453:148–156
- Matthews DK (1970) Roman Aqueducts- Technical aspects of their construction. *Expedition Magazine* 13:2–16, <http://www.penn.museum/sites/expedition/?p=2157>
- McCalpin J (2009) *Paleoseismology*, 2nd edn. Academic Press, Cambridge
- Meghraoui M, Gomez F, Sbeinati R, Van der Woerd J, Mouty M, Darkal A, Radwan Y, Layyous I, Najjar HM, Darawchek R, Hijazi F, Al-Ghazzi R, Barazangi M (2003) Evidence for 830 years of seismic quiescence from paleoseismology, archeoseismology and historical seismicity along the Dead Sea fault in Syria. *Earth Planet Sci Lett* 210:35–52
- Mourabit T, Abou Elenean KM, Ayadi A, Benouar D, Suleman AB (2014) Neo-deterministic seismic hazard assessment in North Africa. *J Seismol* 18:301–318. <https://doi.org/10.1007/s10950-013-9375-2>
- Mucciarelli M, Gallipoli M (2001) A critical review of 10 years of microtremor HVSr technique. *Bollettino Di Geofisica Teorica Ed Applicata* 42:255–266
- Musson R, Grünthal G, Stucchi M (2009) The comparison of macroseismic intensity scales. *J Seismol* 14:413–428. <https://doi.org/10.1007/s10950-009-9172-0>
- Niemi TM (2017) *Archaeoseismology*. In: Gilbert AS (ed) *Encyclopedia of Geoarchaeology*. Encyclopedia of Earth Sciences Series. Springer, Dordrecht. https://doi.org/10.1007/978-1-4020-4409-0_59
- O'Rourke TD, Jeon S-S, Toprak S et al (2014) Earthquake response of underground pipeline networks in Christchurch, NZ. *Earthq Spectra* 30:183–204. <https://doi.org/10.1193/030413EQS062M>
- Passchier CW, Wiplinger G, Güngör T, Kessener P, Gül S (2013) Normal fault displacement displacing a Roman aqueduct of Ephesos, western Turkey. *Terra Nova* 25:292–297. <https://doi.org/10.1111/ter.12035>
- Psycharis IN, Lemos JV, Papastamatiou DY, Zambas C, Papantopoulos C (2003) Numerical study of the seismic behavior of a part of the Parthenon Pronaos. *Earthq Eng Struct Dyn* 32:2063–2084
- Rebai S, Philip H, Taboada A (1992) Modern tectonic stress field in the Mediterranean region: evidence for variation in stress directions at different scales. *Geophys J Int* 110:106–140. <https://doi.org/10.1111/j.1365-246X.1992.tb00717.x>
- Sbeinati MR, Meghraoui M, Suleyman G, Gomez F, Grootes P, Nadeau M-J, Al Najjar H, Al-Ghazzi R (2010) Timing of earthquake ruptures at the Al Harif Roman aqueduct (Dead Sea fault, Syria) from archaeoseismology and paleoseismology. In: Sintubin M, Stewart IS, Niemi TM, Altunel E (eds) *Ancient Earthquakes*. Geological Society of America, Boulder, pp 243–267. [\(Geological Society of America special paper\)](https://doi.org/10.1130/2010.2471(20))

- Schweppe G, Hinzen K-G, Reamer SK, Marco S (2021) Reconstructing the slip velocities of the 1202 and 1759 CE earthquakes based on faulted archaeological structures at Tell Ateret, Dead Sea Fault. *J Seismolog.* <https://doi.org/10.1007/s10950-021-10009-0>
- Stiros S (1988) Archaeology, a tool to study active tectonics. The Aegean as a case study. *Eos Trans Am Geophys Union* 13:1636–1639
- Stiros S (2001) The AD 365 Crete earthquake and possible seismic clustering during the 4–6th centuries AD in the Eastern Mediterranean: a review of historical and archaeological data. *J Struct Geol* 23:545–562
- Stiros S (2020) Monumental articulated ancient Greek and Roman columns and temples and earthquakes: archaeological, historical, and engineering approaches. *J Seismolog* 24:1–29. <https://doi.org/10.1007/s10950-019-09902-6>
- Stiros S, Jones RE (1996) *Archaeoseismology*. British School at Athens, Fitch Laboratory Occasional Paper, Vol. 7
- Sürmelihindi G, Passchier C, Crow J, Spötl C, Mertz-Kraus R (2021) Carbonates from the ancient world's longest aqueduct: a testament of Byzantine water management. *Geoarchaeology* 6:643–659. <https://doi.org/10.1002/gea.21853>
- Tadono T, Ishida H, Oda F, Naito S, Minakawa K, Iwamoto H (2014) Precise Global DEM Generation by ALOS PRISM. *ISPRS Ann Photogramm Remote Sens Spat Inf Sci II*–4:71–76
- Takaku J, Tadono T, Tsutsui K (2014) Generation of high resolution Global DSM from ALOS PRISM. *Int Arch Photogramm Remote Sens Spat Inf Sci XL*–4:243–248 (**ISPRS TC IV Symposium, Suzhou, China**)
- Di Vita, A (1996) Earthquakes and civil life at Gortyn (Crete) in the period between Justinian and Constant II. In: Stiros, S and Jones, R (eds) *Archaeoseismology*. Fitch Lab Occasional Paper 7:45–50
- Volant P, Levret A, Carbon D et al (2009) An archaeo-seismological study of the Nîmes Roman aqueduct, France: indirect evidence for an $M > 6$ seismic event? *Nat Hazards* 49:53–77. <https://doi.org/10.1007/s11069-008-9276-9>
- Wald DJ, Quitoriano V, Heaton TH, Kanamori H (1999) Relationships between peak ground acceleration, peak ground velocity, and modified Mercalli intensity in California. *Earthq Spectra* 15:557–564
- Wang R (1999) A simple orthonormalization method for stable and efficient computation of Green's functions. *Bull Seismol Soc Am* 89:733–741
- Wells DL, Coppersmith KJ (1994) New empirical relationships among magnitude, rupture length, rupture width, rupture area, and surface displacement. *Bull Seismol Soc Am* 84:974–1002
- Worden CB, Thompson EM, Hearne M, Wald DJ (2020) *ShakeMap Manual Online: technical manual, user's guide, and software guide*, U. S. Geological Survey. <http://usgs.github.io/shakemap/>. <https://doi.org/10.5066/F7D21VPQ>

Publisher's Note Springer Nature remains neutral with regard to jurisdictional claims in published maps and institutional affiliations.